Cancer Induces a Stress Ileopathy Depending on β-Adrenergic Receptors and Promoting Dysbiosis that Contributes to Carcinogenesis

Satoru Yonekura[1,2,3], Safae Terrisse[1,2,3], Carolina Alves Costa Silva[1,2,3], Antoine Lafarge[4], Valerio Iebba[1,2,5], Gladys Ferrere[1,2], Anne-Gaëlle Goubet[1,2,3], Jean-Eudes Fahrner[1,2,3], Imran Lahmar[1,2,3], Kousuke Ueda[6], Gibrail Mansouri[2], Eugénie Pizzato[1,2], Pierre Ly[1,2], Marine Mazzenga[1,2], Cassandra Thelemaque[1,2], Marine Fidelle[1,2,3], Fanny Jaulin[7], Jérôme Cartry[7], Marc Deloger[8], Marine Aglave[8], Nathalie Droin[9], Paule Opolon[10], Angélique Puget[11], Fanny Mann[11], Michel Neunlist[12,13], Anne Bessard[12,13], Laetitia Aymeric[13,14], Tamara Matysiak-Budnik[12,13,14,15], Jacques Bosq[16], Paul Hofman[17], Connie P.M. Duong[1,2,18], Sophie Ugolini[19], Valentin Quiniou[20], Sylvie Berrard[21], Bernhard Ryffel[22], Oliver Kepp[4,23], Guido Kroemer[4,23,24,25,26], Bertrand Routy[27,28], Leonardo Lordello[1,2,29], Mohamed-Amine Bani[10], Nicola Segata[30,31], Fjodor Yousef Yengej[32,33,34], Hans Clevers[32,33,34], Jean-Yves Scoazec[3,10], Edoardo Pasolli[35], Lisa Derosa[1,2,3,36], and Laurence Zitvogel[1,2,3,29]

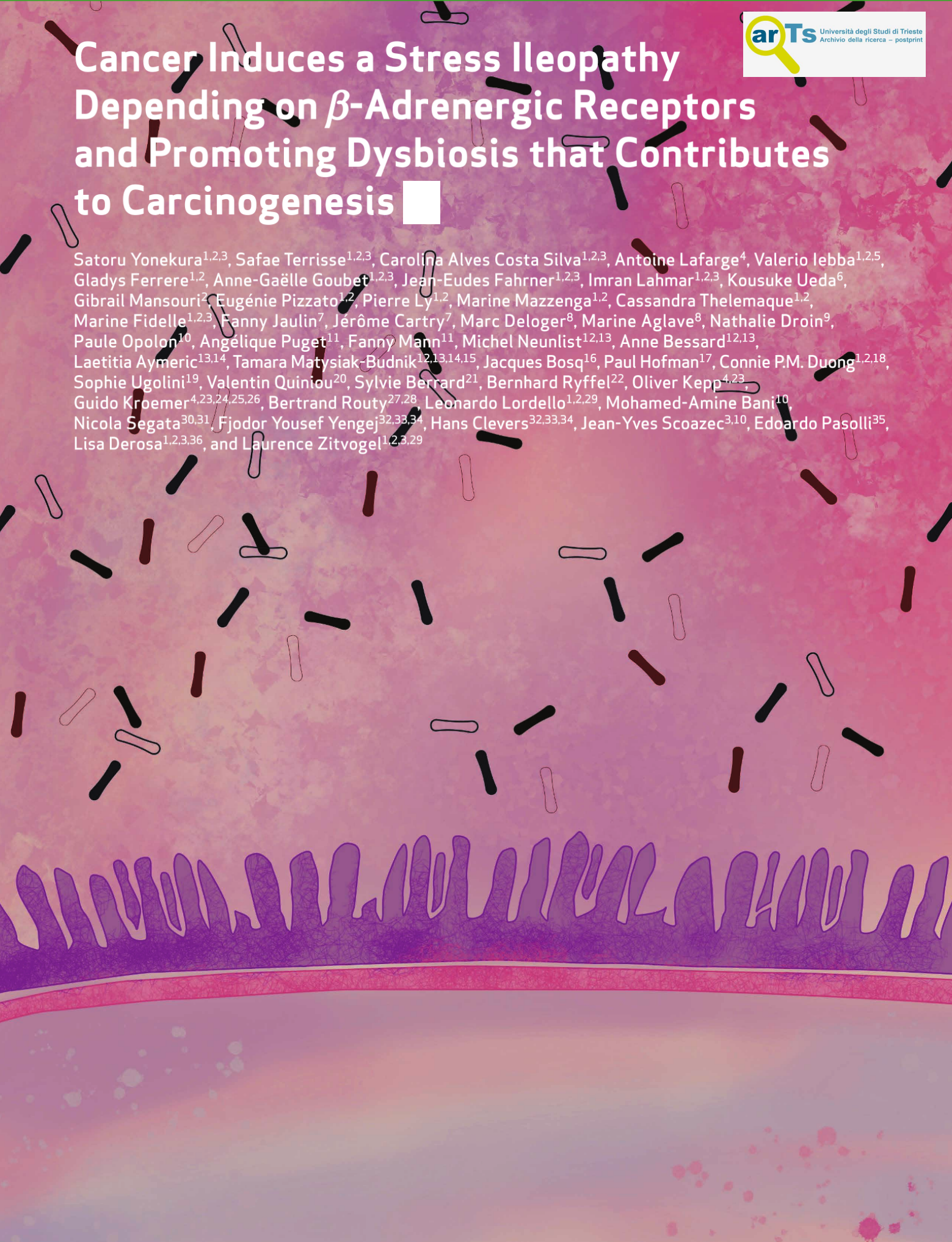

ABSTRACT Gut dysbiosis has been associated with intestinal and extraintestinal malignancies, but whether and how carcinogenesis drives compositional shifts of the microbiome to its own benefit remains an open conundrum. Here, we show that malignant processes can cause ileal mucosa atrophy, with villous microvascular constriction associated with dominance of sympathetic over cholinergic signaling. The rapid onset of tumorigenesis induced a burst of REG3γ release by ileal cells, and transient epithelial barrier permeability that culminated in overt and long-lasting dysbiosis dominated by Gram-positive *Clostridium* species. Pharmacologic blockade of β-adrenergic receptors or genetic deficiency in *Adrb2* gene, vancomycin, or cohousing of tumor bearers with tumor-free littermates prevented cancer-induced ileopathy, eventually slowing tumor growth kinetics. Patients with cancer harbor distinct hallmarks of this stress ileopathy dominated by *Clostridium* species. Hence, stress ileopathy is a corollary disease of extraintestinal malignancies requiring specific therapies.

SIGNIFICANCE: Whether gut dysbiosis promotes tumorigenesis and how it controls tumor progression remain open questions. We show that 50% of transplantable extraintestinal malignancies triggered a β-adrenergic receptor–dependent ileal mucosa atrophy, associated with increased gut permeability, sustained *Clostridium* spp.–related dysbiosis, and cancer growth. Vancomycin or propranolol prevented cancer-associated stress ileopathy.

INTRODUCTION

During the last decade, the gut microbiome has garnered much attention in the context of evolving immuno-oncology, with compelling evidence of the role of intestinal dysbiosis in primary resistance to immune checkpoint blockade across a large range of advanced malignancies (1–4). This contention was supported by numerous epidemiologic studies pointing out the deleterious impact of broad-spectrum antibiotics in the clinical outcome of anti–PD-1/anti–PD-L1 antibodies in stage III and IV melanoma and lung, kidney, and bladder cancers (5, 6). Of note, the decreased richness of the intestinal ecosystem was associated with a tumor microenvironment poor in T-cell infiltrates.

The increased awareness of the potential contribution of gut dysbiosis in treatment failure led many investigators to describe metagenomics (MG)-based intestinal blueprints associated with resistance to immunotherapy (1–3, 7, 8). However, to what extent cancer-associated dysbiosis precedes the tumorigenic process and therefore is causatively linked to neoplasia

[1]Gustave Roussy, ClinicObiome, Villejuif, France. [2]INSERM U1015, Equipe Labellisée – Ligue Nationale contre le Cancer, Villejuif, France. [3]Université Paris-Saclay, Le Kremlin Bicêtre, France. [4]INSERM U1138, Equipe labellisée par la Ligue contre le cancer, Université de Paris, Sorbonne Université, Centre de Recherche des Cordeliers, Paris, France. [5]Department of Medicine, Surgery and Health Sciences, University of Trieste, Trieste, Italy. [6]Department of Urology, Kurume University School of Medicine, Kurume, Japan. [7]INSERM U1279, Gustave Roussy Cancer Campus, Villejuif, France. [8]Bioinformatics Platform, Gustave Roussy Cancer Campus, Villejuif, France. [9]Genomics Platform, Gustave Roussy Cancer Campus, Villejuif, France. [10]Departement of Biology and Medical Pathology, PETRA Platform, Gustave Roussy, Villejuif, France. [11]Aix Marseille University, CNRS, IBDM, Marseille, France. [12]Nantes Université, The Enteric Nervous System in Gut and Brain Disorders (TENS), Institut des Maladies de l'Appareil Digestif (IMAD), Nantes, France. [13]UMR Inserm U1235, TENS, Nantes, France. [14]Department of Biology, Université d'Angers, 44045 Angers, France. [15]Hépato-Gastroentérologie & Oncologie Digestive, IMAD, Hôtel Dieu, CHU de Nantes, Nantes, France. [16]JBO Consultant, Paris, France. [17]Laboratoire de Pathologie Clinique et Expérimental, FHU OncoAge et Biobanque BB-0033-00025, CHU de Nice, Université Côte d'Azur, Nice, France. [18]Department of Medical Biology, University of Melbourne, Melbourne, Victoria, Australia. [19]Centre d'Immunologie de Marseille-Luminy, Université de la Méditerranée, Marseille, France. [20]Parean Biotechnologies, Saint-Malo, France. [21]Université de Paris, Neuro-Diderot, Inserm, Paris, France. [22]UMR 7355, Molecular Immunology and Embryology, CNRS, University of Orleans, Orléans, France. [23]Cell Biology and Metabolomics Platforms, Gustave Roussy Cancer Campus, Villejuif, France. [24]Pôle de Biologie, Hôpital Européen Georges Pompidou, Assistance Publique-Hôpitaux de Paris, Paris, France. [25]Suzhou Institute for Systems Medicine, Chinese Academy of Medical Sciences, Suzhou, China. [26]Department of Women's and Children's Health, Karolinska University Hospital, Karolinska Institute, Stockholm, Sweden. [27]Centre de Recherche du Centre hospitalier de l'Université de Montréal (CRCHUM), Division of Oncology, Department of Medicine Montréal, Quebec, Canada. [28]Centre Hospitalier de l'Université de Montréal (CHUM), Hematology-Oncology Division, Department of Medicine, Montréal, Quebec, Canada. [29]Center of Clinical Investigations in Biotherapies of Cancer (CICBT) 1428, Villejuif, France. [30]Department CIBIO, University of Trento, Trento, Italy. [31]European Institute of Oncology IRCCS, Milan, Italy. [32]Hubrecht Institute-Royal Netherlands Academy of Arts and Sciences and University Medical Center Utrecht, Utrecht, the Netherlands. [33]Department of Nephrology and Hypertension, University Medical Center Utrecht, Utrecht, the Netherlands. [34]Oncode Institute, Utrecht, the Netherlands. [35]Department of Agricultural Sciences, University of Naples Federico II, Portici NA, Italy. [36]Departement of Medical Oncology, Gustave Roussy Cancer Campus, Villejuif, France.

S. Yonekura, S. Terrisse, and C. Alves Costa Silva are the co–first authors of this article.

L. Derosa and L. Zitvogel are the co–last authors of this article.

Corresponding Author: Laurence Zitvogel, ClinicObiome, Gustave Roussy, 114 rue Edouard Vaillant, Villejuif 94805, France. Phone: 33-1-42-11-50-41; Fax: 33-1-42-11-60-94; E-mail: laurence.zitvogel@gustaveroussy.fr

development or is merely its direct consequence remains unknown. Here we show in mice and humans that the tumorigenic process triggers a sustained dysbiosis (in favor of species belonging to the *Clostridium* genus) associated with a stress ileopathy, characterized by ileal mucosa atrophy, constriction of the microvascular villous circulation, and increased expression of tyrosine hydroxylase concomitant with a drop in parasympathetic signaling in the mucosa. Transient amplifying cells and Paneth cells lose their defensins while producing antimicrobial peptides in response to catecholamines. *Clostridia*-killing vancomycin and genetic or pharmacologic inhibition of β-adrenergic receptors interfered in the natural tumor growth kinetics, suggesting that cancer-induced ileopathy should be viewed as a critical corollary of tumorigenesis.

RESULTS

Cancer Can Cause a Terminal Ileopathy

Inflammatory processes distal from the intestine, such as traumatic or ischemic brain injuries, may cause gastrointestinal dysfunction, increased epithelial barrier permeability, and dysbiosis in experimental models and patients (9, 10). Given that cancers are chronic inflammatory lesions, we assessed potential changes in gut permeability following tumor implantation. Transgene-enforced expression of the *Ret* proto-oncogene under control of the metallothionein 1 promoter drives spontaneous melanomagenesis mimicking the human melanoma progression. We took advantage of a *Ret* transgenic melanoma cell line that reaches a surface of 25 to 35 mm^2 within seven days after the subcutaneous inoculation of the minimal tumorigenic dose, leading to tumor outgrowth in 100% cases. We gavaged FITC-labeled dextran (FITC–dextran) into mice at various time points after the inoculation of a sublethal dose of RET melanoma cells (vs. PBS) and determined serum levels of FITC–dextran dye. We observed its transient elevation at 9 days, but not at day 12 after tumor injection, yet less impressive than colitis-induced FITC leakage (Fig. 1A). We also detected blood FITC within six days after inoculation of the transplantable MC38 colon cancer (Supplementary Fig. S1A). Moreover, we found the serum hallmarks of the "leaky gut" syndrome described earlier (11) with elevation of soluble ST2 (IL33R) and/or CD14 at day 20 of RET and/or MCA205 sarcoma tumor bearers (Fig. 1B; Supplementary Fig. S1B) in the absence of weight loss (Supplementary Fig. S1C). This transient gut permeability was accompanied by morphologic changes of the mucosa, starting at day 3, peaking at days 6 to 9, and resolving by day 12 (Fig. 1C). Indeed, a careful examination of tissue sections in light microscopy by four independent pathologists concluded a patchy, partial, or subtotal thickness reduction of the mucosa, characterized by villus atrophy and, in some cases, abrasion of villus extremities, resulting in a significant decrease of the villus/crypt height ratio, bereft of inflammatory infiltrates, in the proximal and terminal ileum (Fig. 1C; Supplementary Fig. S1D). Conversely, IHC staining of $CD8^+$ and $Gr1^+$ cells within the ileal lamina propria (LP) showed reduced intra- and extravascular $CD8^+$ T-cell numbers and LP infiltration by $Gr1^+$ cells following RET inoculation (Supplementary Fig. S1E and S1F). Concomitant changes in the $CD34^+$ villous microvasculature were observed by day 3 (up to day 7), with a significant reduction of the vascular thickness in the distal ileum of RET tumor bearers (Fig. 1D). These morphologic abnormalities spared the duodenum, the jejunum, and colon mucosae (Supplementary Fig. S1G) and were not observed following the injection of killed RET cancer cells (Fig. 1C). The reduction of villus/crypt height ratios coincided with the apoptosis of ileal crypt cells stained with antibodies against cleaved caspase-3 (Fig. 1E), as well as defects in Ki-67^+ proliferative cells at the junction between the transit amplifying compartment and the villus (Fig. 1F). Intestinal epithelial and endothelial cells are normally tightly bound together by intercellular junctional complexes that regulate the paracellular permeability. We stained the ileum of tumor bearers for the tight junction protein Zonula occludens-1 (*Zo1*) and the adherens junction protein E-cadherin but failed to identify an altered distribution during the first three days after RET inoculation (Supplementary Fig. S1H and S1I). In addition, qRT-PCR assessing ileal *Mylk*, *Jam1*, *Ocln*, and *Zo1* gene transcription at day 3 did not show any influence of the tumor establishment (Supplementary Fig. S1J). Of note, tumor inoculation induced a significant decrease of eosinophil numbers in the ileum of RET-bearing mice by day 3 after tumor implantation (Supplementary Fig. S1K). Importantly, this dramatic decrease of the villus/crypt height ratio and occurrence of crypt apoptosis were not only observed by day 3 and up to day 9 after implantation of RET melanoma but were also evidenced after the subcutaneous administration of MCA205 fibrosarcomas and MC38 colon cancers (syngeneic of C57BL/6 mice), but not B16F10 melanoma, nor AT3 or 4T1 breast cancer implantation (Fig. 1G–J). Moreover, orthotopic renal RENCA in the subcapsular area of the kidney of BALB/c mice or lung TC1 within the lung parenchyma both induced the mucosal atrophy at later time points (>day 15), whereas an intravenous model of lung metastases of TC1 failed to do so (Fig. 1G–J).

Altogether, we unveiled that 57% ($n = 4/7$) of mouse transplantable tumors could trigger a cancer-associated ileopathy characterized by a transient (starting at day 3, peaking at days 6–9, and resolving by day 12) epithelial atrophy of the terminal ileum.

Cancer Can Promote Intestinal Dysbiosis in Mice

Intrigued by this cancer-associated ileopathy, we concomitantly analyzed compositional shifts of the fecal microbiota longitudinally in these tumor bearers at different time points of tumor progression across five tumor models. We used high-throughput amplicon sequencing of the gene encoding 16S rRNA and the relevant bioinformatics tools to analyze differences in taxonomic composition in a paired manner, before (D0) and at day 7 (D7) following subcutaneous tumor inoculation across five tumor subtypes (RET, MCA205, RENCA, MC38, and AT3), and we pursued until day 12 (D12) and day 19 (D19) for RET and MCA205 tumors (Fig. 2A and B; Supplementary Fig. S2). There were no differences in any of the alpha diversity metrics inspected (richness, evenness, Shannon index, and Simpson diversity index) at any time point in any of the six tumor types (not shown). However, the principal coordinate analyses (PCoA) of microbial β-diversity distances identified significant shifts in the microbiome composition over time in RET [Fig. 2A for D0 vs. D12; Supplementary Fig. S2A for D0 vs. D7 (top) and

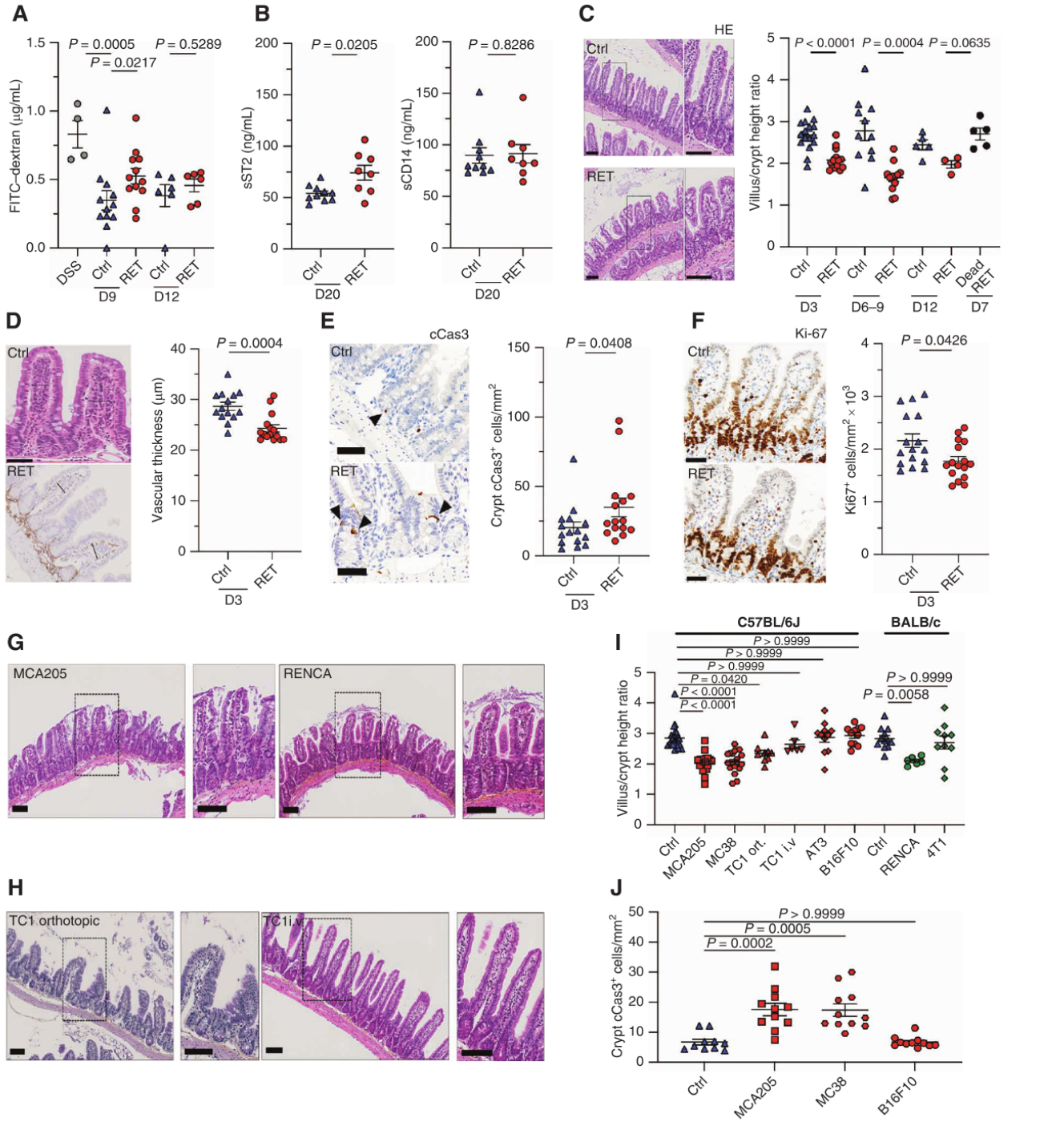

Figure 1. Prototypic pathologic features of cancer-associated ileopathy. **A,** RET-induced (right) or DSS-induced (left) intestinal permeability monitored by FITC–dextran oral administration at day 9 or 12 and translocation in the bloodstream 4 hours later. Each dot represents one mouse; one representative experiment out of two is depicted. Mann–Whitney test was used for comparison with the control group. DSS, dextran sulfate sodium. **B,** Plasma levels of soluble CD14 and ST2 at day 20 in naïve versus RET tumor bearers. Two concatenated experiments are plotted. Each dot represents one mouse. Mann–Whitney test was used for comparison with the control group. **C,** Morphologic changes. Left, typical micrograph of hematoxylin/eosin/saffron-stained ileal tissue visualized in light microscopy. Scale bar, 100 µm (Ctrl: PBS injection, RET: tumor injection). Right, manual calculation of the villus/crypt height ratio in the distal ileum, at day 3, days 6–9, and day 12, after subcutaneous tumor implantation of live or dead RET (day 7) versus PBS. Each dot represents one mouse in two concatenated independent experiments of 4–6 mice/group. Mann–Whitney test was used for comparison with the control group. **D,** CD34 staining to monitor villous vascular thickness. A prototypic micrograph picture is shown followed by precise measurement of vascular thickness in RET- and PBS-injected mice at day 3. Each dot represents the mean of 30 ileal villi/animals. Mann–Whitney test was used for comparison with the control group. **E** and **F,** Typical micrograph picture of ileal crypts (**E**) or whole epithelia (**F**) stained with anti-cleaved caspase-3 (cCas3) Ab (**E**) or anti-Ki-67 Ab (**F**; positivity outlined in black arrows) in naïve Ctrls (PBS injection) or RET tumor bearers at day 3, and manual calculation for cCas3 and automated quantification of Ki-67–positive cells/mm^2 were performed. Scale bar, 50 µm. Mann–Whitney test was used for comparison with the control group. **G–J,** The same as **C** and **E**, but subcutaneous implantation of different tumor cell lines (MCA205, MC38, B16F10, AT3, orthotopic or intravenous (i.v.) TC1, syngeneic of C57BL/6 mice, or orthotopic RENCA, 4T1 syngeneic of BALB/c mice). Each graph assembles results from 1to 3 independent experiments containing groups of 5–6 mice sacrificed at day 7 after subcutaneous tumor implantation or days 15–21 for orthotopic or i.v. TC1 or RENCA. ANOVA statistical analyses (Kruskal–Wallis test) were used for multiple comparisons. Numerical *P* values are indicated.

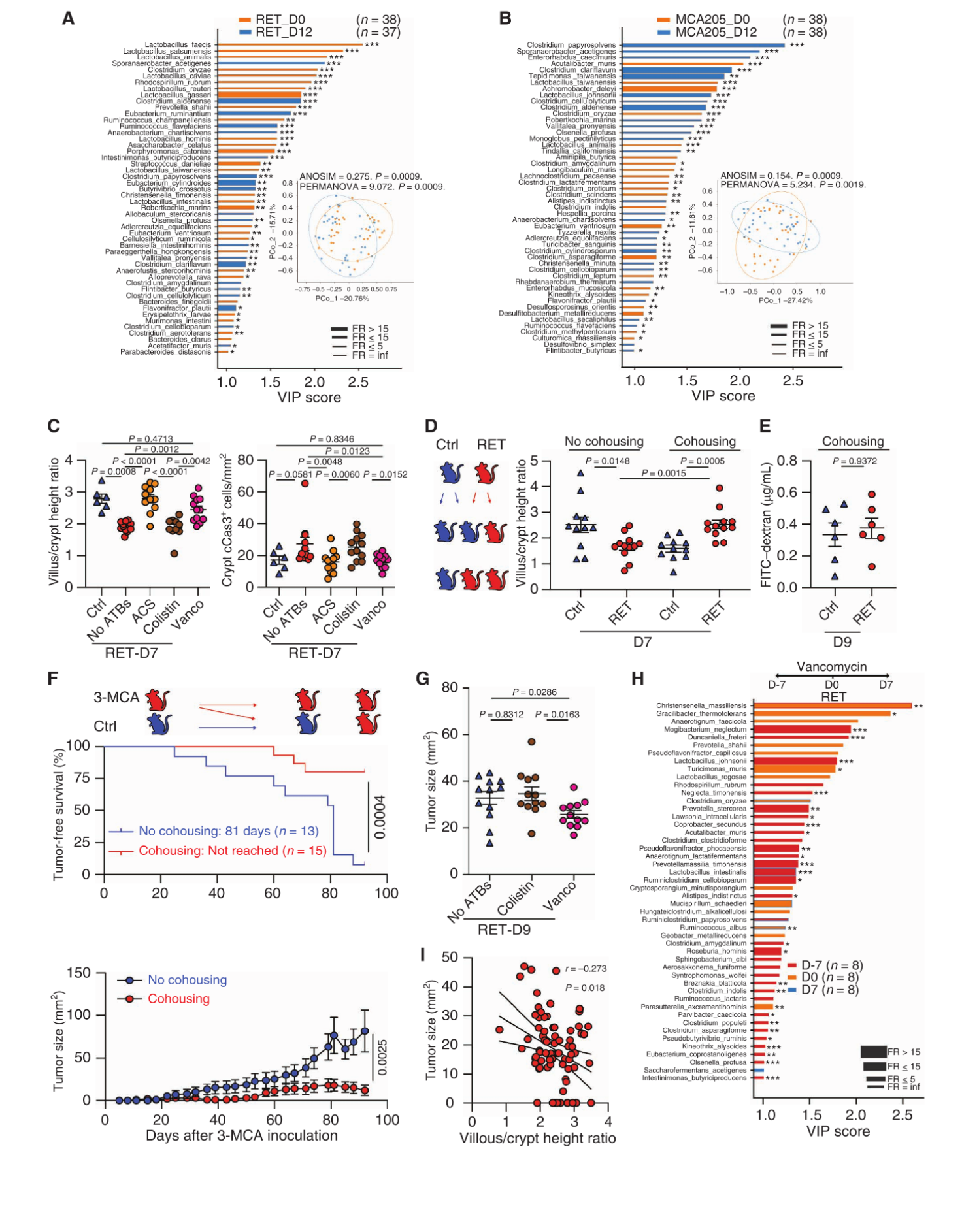
A
RET_D0 (n = 38)
RET_D12 (n = 37)
ANOSIM = 0.275. P = 0.0009.
PERMANOVA = 9.072. P = 0.0009.
PCo_2 −15.71%
PCo_1 −20.76%
FR > 15
FR ≤ 15
FR ≤ 5
FR = inf
VIP score
B
MCA205_D0 (n = 38)
MCA205_D12 (n = 38)
ANOSIM = 0.154. P = 0.0009.
PERMANOVA = 5.234. P = 0.0019.
PCo_2 −11.61%
PCo_1 −27.42%
VIP score
C
Villus/crypt height ratio
Crypt cCas3+ cells/mm2
P = 0.4713
P = 0.0012
P < 0.0001
P = 0.0042
P = 0.0008
P < 0.0001
P = 0.8346
P = 0.0123
P = 0.0048
P = 0.0581
P = 0.0060
P = 0.0152
Ctrl
No ATBs
ACS
Colistin
Vanco
RET-D7
D
Ctrl
RET
No cohousing
Cohousing
P = 0.0148
P = 0.0005
P = 0.0015
Villus/crypt height ratio
D7
E
Cohousing
P = 0.9372
FITC−dextran (μg/mL)
D9
F
3-MCA
Ctrl
Tumor-free survival (%)
No cohousing: 81 days (n = 13)
Cohousing: Not reached (n = 15)
0.0004
Tumor size (mm2)
No cohousing
Cohousing
0.0025
Days after 3-MCA inoculation
G
Tumor size (mm2)
P = 0.0286
P = 0.8312
P = 0.0163
No ATBs
Colistin
Vanco
RET-D9
H
Vancomycin
D-7
D0
D7
RET
D-7 (n = 8)
D0 (n = 8)
D7 (n = 8)
FR > 15
FR ≤ 15
FR ≤ 5
FR = inf
VIP score
I
Tumor size (mm2)
r = −0.273
P = 0.018
Villous/crypt height ratio

D0 vs. D19 (bottom)], MCA205 [Fig. 2B for D0 vs. D12; Supplementary Fig. S2B for D0 vs. D7 (top), D0 vs. F4 (bottom)], and RENCA tumor models (between D0 and D7; Supplementary Fig. S2C), coinciding with ileal atrophy. In contrast, no significant compositional modulations of the stools could be observed in AT3 tumor bearers (between D0 and D7; Supplementary Fig. S2D) in accordance with the absence of ileopathy. To determine the relative contribution of the abundance of each bacterial species at D0 to the observed group separation at D12, bacterial species were ordered according to their variable importance (VIP) score [which relies on the supervised analysis of partial least square discriminant analysis (PLS-DA); Fig. 2A (RET) and Fig. 2B (MCA205)]. We found a common relative dominance of the Clostridiales order (including *Clostridiaceae* family members, i.e., *Clostridium papyrosolvens*, *C. clariflavum*, *C. cellulolyticum*, *C. aldenense*, and *C. cellobioparum*; *Ruminococcaceae* family members, such as *R. flavefaciens* and *F. plautii*; *Sporanaerobacter* genus, such as *S. acetigenes* and *Vallitaleaceae* family members such as *V. pronyensis*) at the expense of *Lactobacillus* genus (relative loss of *L. animalis* and *L. taiwanensis*) across the three ileopathy-promoting tumor types (RET, MCA205, and RENCA; Fig. 2A and B; Supplementary Fig. S2E–S2G). Importantly, in contrast to the transient nature of the cancer-associated ileopathy, cancer-induced gut dysbiosis persisted for a prolonged period (until animal sacrifice at day 19), with the relative overrepresentativity of distinct taxonomic species such as *F. plautii*, *C. papyrosolvens*, *C. clariflavum*, *C. cellulolyticum*, and *S. acetigenes* and the consistent loss of *Lactobacilli* spp. and *C. oryzae* or *E. ventriosum* (Supplementary Fig. S2E and S2F).

Hence, we conclude that in one model out of two, cancer could trigger a transient ileopathy associated with a protracted intestinal dysbiosis favoring families and species from the *Clostridium* genus until death.

Significance of Intestinal Dysbiosis in Cancer

To parse out the biological significance of these microbial shifts observed right after tumor inoculation and persisting overtime, we used three orthogonal experimental strategies. First, we analyzed the effects of various antibiotic (ATB) regimens on the RET-induced epithelial atrophy observed at day 7. The broad-spectrum ATB cocktail ampicillin, colistin, and streptomycin (ACS) as well as vancomycin (expected to kill most Gram-positive bacteria) completely prevented the reduction of the ileal villus/crypt height ratio and crypt cell apoptosis (Fig. 2C, left and right plots), whereas colistin (only killing Gram-negative commensals) failed to do so, supporting a role for Gram-positive *Clostridium spp.* in this ileopathy. Second, the cohousing of RET tumor bearers with tumor-free mice together for six to nine days (Fig. 2D, left) revealed transmission patterns because it created an ileopathy of the distal ileum in "healthy" animals while significantly protecting the RET tumor–bearing littermates from ileum epithelial damage (Fig. 2D, right). Moreover, cohousing also prevented the transient increase of gut permeability to FITC–dextran dye at nine days after RET tumor implantation (Figs. 1A and 2E). Third, to show the causal link between gut dysbiosis and tumor incidence, we inoculated the 3-methycholanthrene (3-MCA) chemical carcinogen capable of inducing fibrosarcoma in 100% naïve C57BL/6 mice at a dosing of 100 μg (12) and compared the incidence and severity of tumor development in 3-MCA recipients maintained alone or together with healthy littermates that did not receive the carcinogen (Fig. 2F, top). Surprisingly, fibrosarcoma formation was significantly retarded and exhibited slower growth kinetics (Fig. 2F, bottom) in animals reared with healthy controls as compared with 3-MCA–isolated animals. Finally, we concluded the preclinical significance of ileopathy-associated dysbiosis in cancer by showing a transient tumor growth retardation induced by the prophylactic oral administration of vancomycin (Fig. 2G). Vancomycin coincided with the relative underrepresentation of six *Clostridia spp.* (*C. clostridioforme*, *C. asparagiforme*, *C. indolis*, *C. populeti*, *C. ihumi*, and *C. amygdalinum;* Fig. 2H; Supplementary Fig. S2H) and with the relative reemergence of distinct Lactobacilli (such as *Lactobacillus rogosae)*. Finally, the cause–effect relationship

Figure 2. Microbiota-dependent cancer-induced ileopathy and biological significance. **A** and **B,** PCoA of the taxonomic composition of feces (inset) in a paired manner in naïve versus RET (**A**) or MCA205 (**B**) tumor-bearing mice at day 12 after tumor implantation. β-Diversity of fecal microbiota (bacterial relative abundance) according to time [before (orange) and 12 days after (blue) tumor inoculation]. ANOSIM and PERMANOVA define the separation of the groups; *P* values define the significance of group separation after 999 permutations of the samples. Bar plot of fecal species that discriminate between pre- and post–tumor inoculation in mice, ordered by their variable importance (VIP) score. For each species, the bar color depicts the cohort with the highest mean relative abundance for a defined species, whereas the border color indicates the cohort with the lowest mean relative abundance. An absent border indicates mean relative abundance of zero in comparator cohort(s). Mann–Whitney test was used. Bar thickness reports the fold ratio (FR) value of the mean relative abundances for each species among the two cohorts. **C,** Effects of various types of antibiotics (ATB) regimen on cancer-induced ileal atrophy and apoptosis in ileal crypts. Calculation of the villus/crypt height ratio (left) or crypt apoptosis (right) at day 7 after subcutaneous RET implantation (vs. PBS) was performed. ANOVA statistical analyses (Kruskal–Wallis test) were used for multiple comparisons. Numerical *P* values are indicated. **D** and **E,** Effects of cohousing of tumor bearers with tumor-free mice on ileal morphology and permeability. Calculation of the villus/crypt height ratio in the distal ileum at days 6–9 after RET implantation (vs. PBS) in isolated versus cohoused mice (middle). Each dot represents one mouse. Gut permeability assessed using the same procedure as the one described in Fig. 1A (**E**). Mann–Whitney test was used for comparison with the control group. **F,** Effects of cohousing of tumor bearers with tumor-free mice on tumor incidence and growth kinetics. Experimental setting of 3-MCA–induced tumorigenesis (**F**, top). MCA was injected in isolated mice or mice doomed to be littermates for >90–100 days with naïve C57BL/6 mice in the same cage. Time to tumor incidence (**F**, middle) and tumor growth kinetics over time (**F**, bottom). Survival curves were estimated using the Kaplan–Meier product limit method. **G,** Effects of various types of ATB regimen on tumor size 7 days after tumor inoculation. Each graph assembles results from two independent experiments containing groups of 5–6 mice. ANOVA statistical analyses (Kruskal–Wallis test) were used for multiple comparisons. Numerical *P* values are indicated. **H,** 16S rRNA-based MG sequencing of fecal amplicons before (D −7) and after 7 (D = 0) or 14 (D7) days of vancomycin. Using PLS-DA VIP plot, coupled to a pairwise comparison of relative taxonomic abundances (for species having a prevalence equal to or greater than 5%), we analyzed taxonomic composition differences between the groups treated or not with oral vancomycin. Bar plot of fecal species that discriminate between pre- and post–tumor inoculation in mice, ordered by their VIP score. For each species, the bar color depicts the cohort with the highest mean relative abundance for a defined species, whereas the border color indicates the cohort with the lowest mean relative abundance. An absent border indicates mean relative abundance of zero in comparator cohort(s). Bar thickness reports the FR value of the mean relative abundances for each species among different groups. **I,** Spearman correlation between villus/crypt height ratio in the distal ileum at days 6–9 after RET implantation and tumor size. Each dot represents one mouse/tumor. Four experiments comprising 5–6 mice/group are concatenated.

between the RET-induced overrepresentation of *Clostridia spp.* and reduced tumor immunosurveillance was brought to us by gavaging tumor-bearing mice treated with anti–PD-1 mAb with distinct *Clostridia spp.* associated with antibiotics- and tumor-induced immunosuppression such as *C. hathewayi* and *C. clostridioforme* (5). This oral feeding with cancer-associated *Clostridia spp.* significantly compromised the efficacy of the immunotherapy, whereas *Lactobacillus reuteri* failed to do so (Supplementary Fig. S2I, left and right). Finally, there was a strong correlation between tumor size at day 7 and villus/crypt height ratios (Fig. 2I), supporting the contention that ileopathy is a corollary syndrome of the tumorigenic process.

Hence, cancer-associated ileopathy coincides with a rapid and durable intestinal dysbiosis dominated by Gram-positive *Clostridium* species participating in the aggressiveness of tumor outgrowth.

Cancer Induced Severe Perturbations of Secretory Cells from the Ileum

Using single-cell RNA sequencing, we profiled 44,807 individual epithelial cells from mouse small intestine harvested in naïve and RET tumor bearers at 24 hours after tumor implantation and characterized the gene signatures associated with melanoma inoculation (Fig. 3A). Unsupervised clustering of the leukocytic and epithelial cells partitioned the data into 20 and 25 groups, respectively (Supplementary Fig. S3A and S3B), which we visualized using *t*-stochastic neighborhood embedding and labeled *post hoc* by the expression of reported marker genes (13). Each cluster was associated with a distinct cell type, including epithelial [stem cells, enterocytes, goblet, Paneth, enteroendocrine (EEC) secretory cells, and tuft cells] and immune cells (T, B, dendritic, and macrophages). Although absorptive enterocytes were partitioned across several clusters representing distinct maturation stages, the EECs, transit amplifying (TA) cells, Paneth, goblet, stem, and tuft cells were each represented by a single distinct cluster (Supplementary Fig. S3A). The proportions of most differentiated ileal cell types were consistent with expected abundances (13) and weakly varied between tumor bearers and naïve animals (Supplementary Fig. S3A–S3C; Supplementary Fig. S4A and S4B), except for nondividing $CD4^+$ T cells ($IL7R^+$, $ICOS^+$, and $RORA^+$), and granzyme A–producing γδ T cells ($CD8a^+$, $CCR6^+$, $KLRD1^+$, and $CCL5^+$) that increased by day 1 after RET inoculation (Supplementary Fig. S4B–S4D), whereas stem and secretory cells were markedly reduced (Fig. 3B). The volcano plot indicating significance versus fold changes of overall versus cell-specific gene expression between naïve and tumor bearers highlighted the relative overexpression of antimicrobial peptides [such as regenerating islet-derived protein 3 beta or gamma (*Reg3β*, *Reg3γ*)] at the expense of defensins (*Defa 5*, *21*, *22*, *23*, *24*, *36*, and *38*) across many clusters of cells (including TA and Paneth cell clusters; Fig. 3C and D), as well as γδT cells and macrophages (Supplementary Fig. S4D and S4E). IHC confirmed the degranulation of distinct crypt cells that encompass Paneth cells and EECs, only in mice bearing tumors triggering the epithelial atrophy (Fig. 3E). Here again, crypt degranulation was a proxy of ileal villus atrophy and prevented by vancomycin (Fig. 3F). We corroborated by qPCR analysis that lectin *Reg3γ* transcription was upregulated at day 7 in the ileal epithelium of RET tumor bearers (Fig. 3G, left) but that antibiotics (broad spectrum and vancomycin but not colistin) could blunt *Reg3γ* gene expression, in line with the capacity of this antimicrobial peptide to bind the peptidoglycan layer of Gram-positive bacteria (14). Lectin *Reg3γ* correlated with epithelial villus atrophy and crypt apoptosis (Fig. 3G, middle and right). In fact, after a transient loss at day 1, EECs defined as chromogranin A–positive (CgA^+) cells were significantly increased by day 3 in the ileal crypts of animals inoculated with tumor cells inducing ileopathy (RET, MCA205, and MC38; Supplementary Fig. S3C; Fig. 4A) but not in animals inoculated with tumors that did not induce crypt damage, such as B16F10 (Fig. 4A, right). Crypt CgA^+ cell numbers correlated with ileal villus atrophy, crypt apoptosis (Fig. 4B), and *Reg3γ* expression (Fig. 4C). Once again, RET-induced early accumulation of EECs capable of overexpressing serum amyloid A gene product (associated with acute inflammation) in ileal crypts was abrogated by vancomycin (Fig. 4D and E) and correlated with tumor size at day 7 (Fig. 4F).

Cancer Induces Catecholamine-Associated Stress Ileopathy

Stress generated by psychological or pathologic disorders can induce most of the features described in this cancer-associated ileopathy (such as increased gut permeability, dysbiosis, and pathophysiologic exacerbation; refs. 10, 15). Despite the potential relevance of the hypothalamic–pituitary–adrenal axis in intestinal permeability (16), we ruled out a role for cancer stress-induced corticosteroids in our symptomatology in as much as corticosterone levels remained stable over time during tumor progression (Supplementary Fig. S5A).

Figure 3. Single-cell transcriptomics analyses reveal acute reactivities of secretory cells. **A,** Single-cell transcriptomics of the CD45-negative component of the terminal ileal epithelial layer overlapping PBS versus RET-injected mice. Uniform manifold approximation and projection (UMAP) plots of $N = 36{,}891$ single cells (points) colored by clusters annotated *post hoc* (refer to Supplementary Fig. S3A) for three naïve and three RET tumor bearers at day 1 after inoculation. Refer to Supplementary Fig. S3A for overlapping representation of the concatenated results for the CD45-positive component of the terminal ileal epithelial layer for the two groups of mice. **B,** Relative proportions of stem cells, neuroendocrine and Paneth cells, and TA cells (according to clusters defined in Supplementary Fig. S3A) in controls (PBS) versus RET-inoculated mice within the CD45-negative fraction. **C** and **D,** Volcano plots of differential gene-expression patterns between pre- and 24 hours after RET inoculation according to $\log_{10}$ adjusted *P* values and $\log_2$ fold ratios for the cluster related to TA cells (**C**, $N = 305$ cells "Ctrl without tumor" vs. $N = 263$ cells "RET") and Paneth cell subsets (**D**, $N = 86$ cells "Ctrl without tumor" vs. $N = 35$ cells "RET") identified from the droplet-based data sets for regional (distal ileum) samples. Significant differences are annotated in red. **E** and **F,** Representative images of degranulating crypts in MCA205 tumor bearers and effects of ATB. Scale bars, 50 μm. Cell degranulation analyzed in hematoxylin/eosin/saffron staining in the ileal crypts of naïve or RET, MCA205, or AT3 tumor bearers at day 7 after tumor inoculation without ATB (**E**) and with ATB (**F**). Each dot corresponds to the enumeration of the percentages of degranulated crypts/5–6 fields/animal (**F**). Symbols represent individual mice. Mann–Whitney test. **G,** Quantitative PCR determination of *Reg3γ* gene transcription in the terminal ileum of RET tumor bearers treated with 7 days of various ATB regimen and correlations with morphologic changes. Spearman correlations between the villus crypt height ratio (middle) and crypt apoptosis (right) and *Reg3γ* gene expression. Each dot represents one ileum. The graph depicts two experiments of 5–6 mice/group, each dot representing one ileum. ANOVA statistical analyses (Kruskal–Wallis test) were used for multiple comparisons. Numerical *P* values are indicated between individual ATB groups versus nontreated controls.

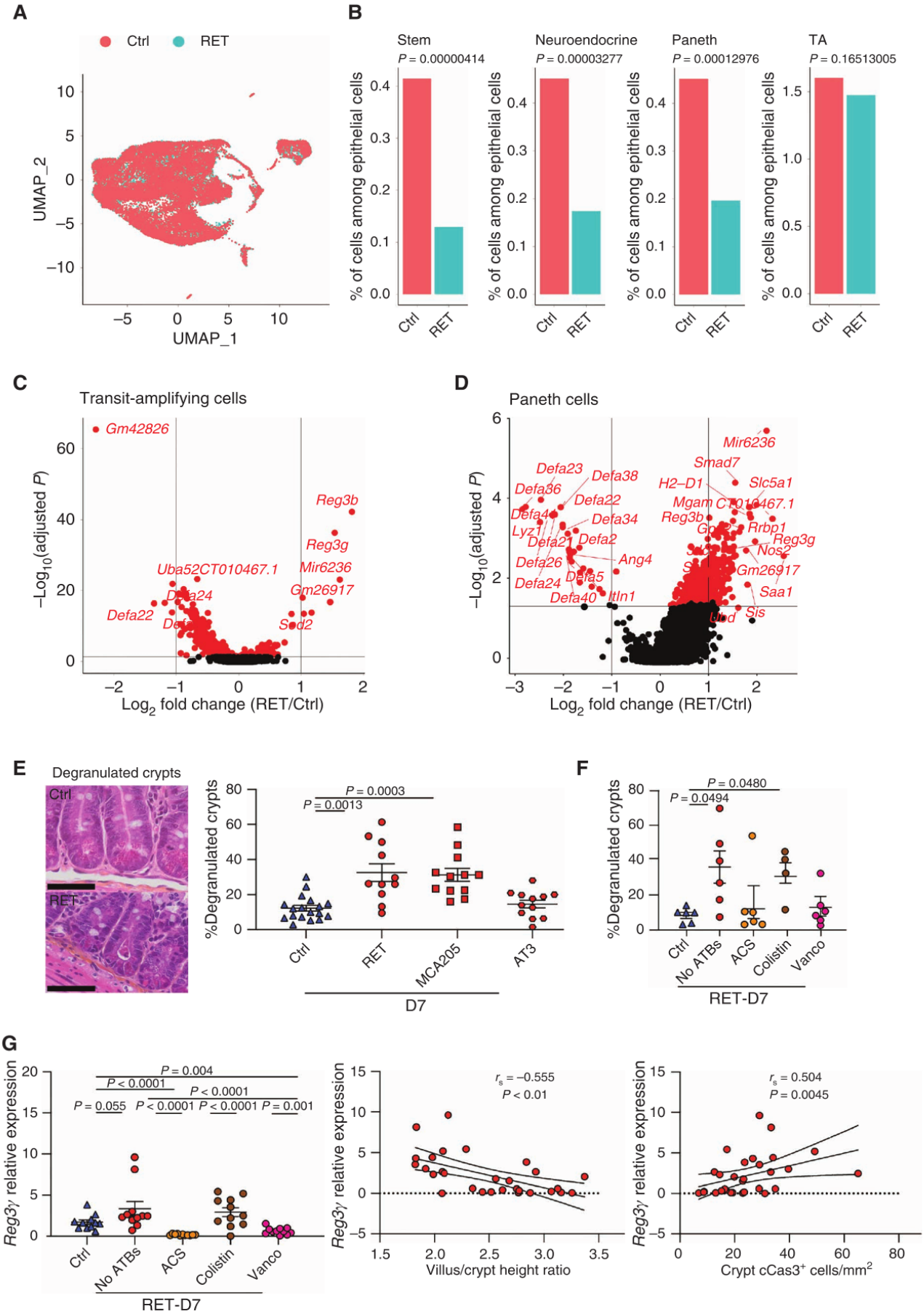
A
Ctrl
RET
UMAP_2
UMAP_1
B
Stem
P = 0.00000414
Neuroendocrine
P = 0.00003277
Paneth
P = 0.00012976
TA
P = 0.16513005
% of cells among epithelial cells
Ctrl
RET
C
Transit-amplifying cells
Gm42826
Reg3b
Reg3g
Uba52CT010467.1
Mir6236
Gm26917
Defa24
Defa22
Sod2
−Log10(adjusted P)
Log2 fold change (RET/Ctrl)
D
Paneth cells
Mir6236
Smad7
Defa23
Defa38
Slc5a1
Defa36
H2–D1
Defa22
Mgam CT010467.1
Defa4
Reg3b
Defa34
Lyz1
Rrbp1
Defa21
Defa2
Reg3g
Defa26
Ang4
Nos2
Defa5
Gm26917
Defa24
Defa40
Itln1
Saa1
Sis
−Log10(adjusted P)
Log2 fold change (RET/Ctrl)
E
Degranulated crypts
Ctrl
RET
%Degranulated crypts
P = 0.0003
P = 0.0013
Ctrl
RET
MCA205
AT3
D7
F
%Degranulated crypts
P = 0.0480
P = 0.0494
Ctrl
No ATBs
ACS
Colistin
Vanco
RET-D7
G
Reg3γ relative expression
P = 0.004
P < 0.0001
P < 0.0001
P = 0.055
P < 0.0001
P < 0.0001
P = 0.001
Ctrl
No ATBs
ACS
Colistin
Vanco
RET-D7
rs = −0.555
P < 0.01
Villus/crypt height ratio
rs = 0.504
P = 0.0045
Crypt cCas3+ cells/mm2

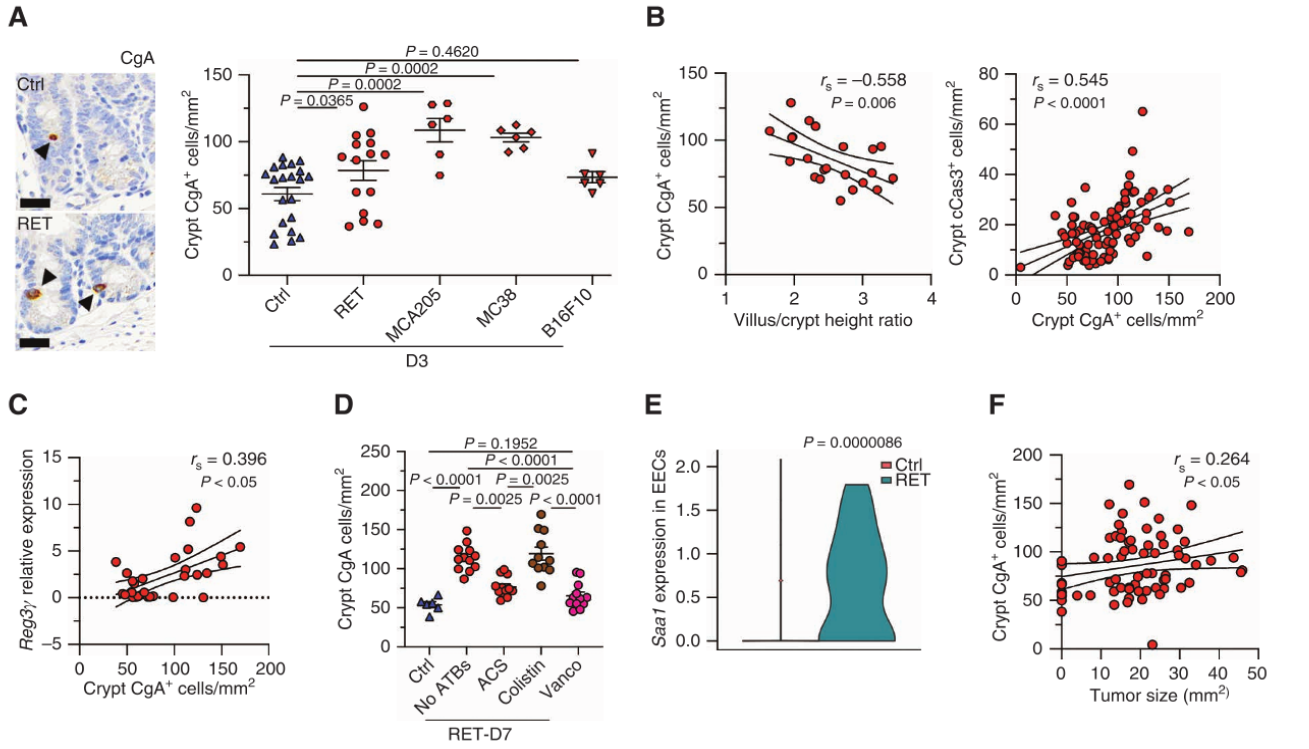

Figure 4. Cancer-induced hyperplasia of EECs in the ileal crypts. **A,** IHC of crypt cells using a CgA-specific staining. Representative micrographs of CgA$^+$ cells in the RET model (left) and enumeration of CgA$^+$ cells/mm^2 in the distal ileum at day 3 after tumor inoculation of different transplantable murine cancers inducing or not inducing ileopathy (right). Scale bar, 25 µm. Mann–Whitney test was used for comparison versus control group. **B** and **C,** Spearman correlations between crypt CgA$^+$ cells and villus/crypt height ratio (**B**, left) or cCas3 (**B**, right) in the RET tumor model or with *Reg3γ* ileal gene expression in qPCR at day 3 after RET implantation (**C**). **D,** Enumeration of ileal crypt CgA$^+$ cells according to various regimens of antibiotics at day 7 in the RET model. ANOVA statistical analyses (Kruskal–Wallis test) were used for multiple comparisons. Numerical *P* values are indicated. **E,** Selective overexpression of the *Saa1* gene product in ileal EECs post-RET inoculation identified in single-cell RNA sequencing of the cluster 22 corresponding to EECs (Supplementary Fig. S3A). **F,** Spearman correlations between crypt CgA$^+$ cells and tumor size at day 7. Each dot represents one mouse. Each graph assembles results from 1 to 3 independent experiments containing groups of 5–6 mice.

The gastrointestinal tract is highly innervated by both intrinsic (enteric) and extrinsic nerve fibers, which provide control of gut functions (17). The intrinsic enteric nervous system is organized in two distinct networks, the submucosal and the myenteric plexuses (17). We performed a quantitative analysis of the densities of nerve fibers of the sympathetic and parasympathetic nervous systems of ileal plexus, submucosae, and mucosae after RET tumor inoculation, using IHC staining with anti–tyrosine hydroxylase (TH), anti–choline acetyltransferase (ChAT), or anti–vesicular acetylcholine transporter (VAChT) antibodies. TH catalyzes the rate-limiting step in the synthesis of catecholamines, whereby L-tyrosine is converted into L-DOPA and then dopamine, which is the precursor of the biogenic amines norepinephrine and epinephrine, all three being important neurotransmitters. In the nervous system, TH is a specific marker of catecholaminergic neurons, whereas ChAT, the ACh-synthesizing enzyme, and VAChT are specifically expressed in cholinergic neurons. ChAT staining was not reliable in IHC. So, we took advantage of the ChAT-eGFP mouse model (18), allowing the fluorescence identification of ileal parasympathetic nerves, as well as cells from the villi, crypts, and stroma of the mucosa. ChAT expression was decreased in the stroma at day 3 after RET inoculation (Fig. 5A). VAChT-immunoreactive nerve fibers that extend into LP inside each villus were clearly reduced by RET injection by day 3 up to days 6 to 9 (Fig. 5B). Of note, ChAT$^+$ cell bodies and fibers were not affected in the ileal myenteric plexus (Supplementary Fig. S5B). Although we failed to observe any changes of TH staining in fibers of the submucosae and myenteric plexus (Supplementary Fig. S5C), we noticed an increase in the density of TH$^+$ cells at the bottom of the ileal crypts that were not bona fide neuronal cells in RET and MCA205 tumor bearers (Fig. 5C). Publicly available transcriptomics data sets reveal selective TH expression in EECs (Supplementary Fig. S5D; ref. 13). TH and CgA single stainings markedly correlated (Fig. 5D). Once again, the RET-induced accumulation of TH-positive cells was abrogated by vancomycin but not colistin (Fig. 5E). Of note, the intrinsic innervation of melanoma tumors associated or not with an ileopathy did not differ (Supplementary Fig. S5E).

Transcription patterns of various genes encoding defensins, antimicrobial peptides, innate interferons, ChAT, and adrenergic receptor signaling suggested a coordination between REG3γ and catecholamine pathways (Supplementary Fig. S5F). Hence, we surmised that biogenic amine neurotransmitters could participate in ileal damage. We incubated mouse 3-D crypt stem cell–derived ileal enteroids with physiologic concentrations of dopamine, noradrenaline, and adrenaline for 24 hours and observed a clear reduction of enterocyte proliferation (Fig. 5F and G), concomitant to an increased secretion of the antimicrobial peptide REG3γ (Fig. 5G). Using human ileal enteroids derived in culture medium allowing the differentiation of secretory

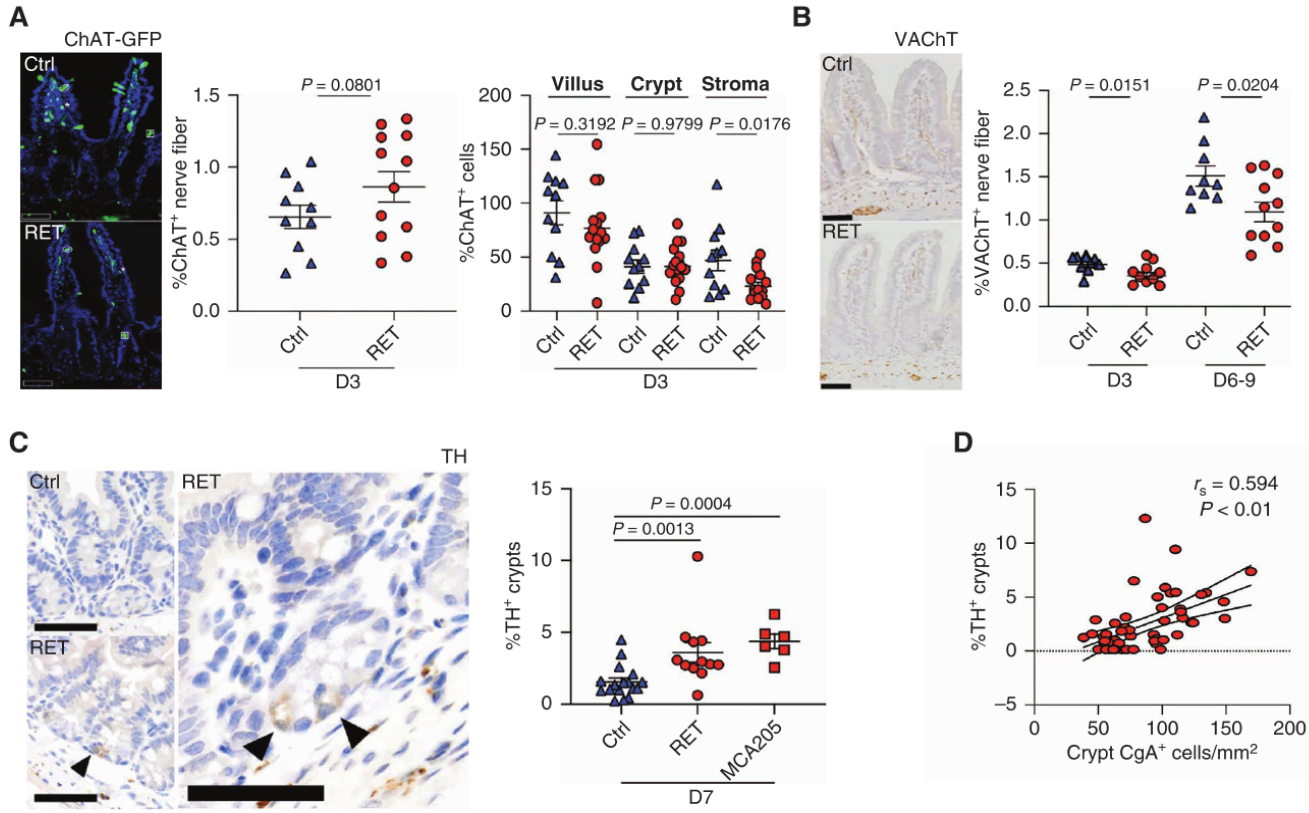

Figure 5. Imbalance between the sympathetic and parasympathetic tonus in ileal mucosa during tumor growth. **A,** ChAT assessment by fluorescence microscopy in the various cell types of the ileal mucosa in eGFP-ChAT transgenic mice after RET (or PBS) inoculation at day 3. ChAT$^+$ nerve fibers (GFP$^+$) were evaluated in the mucosa and submucosa of distal ileum. Also, ChAT$^+$ cells identified in the lining of villi (circle) or crypts (square) and scattered in the stroma "endothelial and immune cells" (star) were counted. Submucosal ganglion cells were excluded from evaluation of ChAT$^+$ nerve fibers and cells. Mann–Whitney test was used for comparison versus control group. **B,** VAChT IHC staining of the ileal mucosa and submucosa using specific antibodies in PBS or RET-injected mice at day 3. One representative micrograph picture (scale bar, 50 μm; **A**, **B**) and counting of positive area/total area in the distal ilea at day 3 (**B**). Each dot represents one mouse. A representative experiment out of two yielding similar conclusions is shown. Mann–Whitney test was used for comparison versus control group. **C,** IHC staining of crypt cells with anti-tyrosine hydroxylase (TH)–specific antibodies with two representative micrograph pictures at two different field of magnification (scale bars, 50 μm), showing that TH$^+$ cells might correspond to Paneth cells or EEC. Enumeration of TH$^+$ cells in ileal crypts at day 3 after tumor inoculation (RET, MCA205; **C**, right). Mann–Whitney test was used for comparison versus control group. **D,** Spearman correlation between % TH$^+$ crypts and CgA$^+$ cells in the ileal crypts in RET-bearing hosts. (*continued on next page*)

cells, we could recapitulate the capacity of epinephrine (and to some extent norepinephrine) to induce the transcription of *REG3G* gene (but not that of defensin genes; Fig. 5H). Of note, *DEFA5* gene expression remained equal or decreased in similar conditions. Incidentally, the RNA sequencing of all LP leukocytes unveiled that the nondividing CD4$^+$ T-cell subset expressing *Icos* and *Rora* gene products contained signal transduction modules compatible with catecholamine stimulation post–RET inoculation (Supplementary Fig. S4C).

Altogether, an imbalance between catecholamine and cholinergic signaling within the ileal mucosa of tumor bearers was a hallmark of cancer-induced ileal damage that may be apostrophed "stress ileopathy."

Cancer-Induced Ileopathy Is Reduced by Pharmacologic Inhibition or Genetic Ablation of β-Adrenergic Receptors and Contributes to Tumor Growth

Previous studies using models of stroke (10), acute kidney ischemia (19), and sepsis (20) have implicated gut-derived norepinephrine as a key mediator of hepatic and systemic inflammation, with a role of α- or β-adrenoreceptors in the pathology exacerbation. We utilized pharmacologic inhibitors of various receptors of the autonomous nervous and endocrine systems (Fig. 6A) as well as gene-deficient mice to nail down which neuroepithelial circuitry could be involved in the cancer-induced ileopathy. Although pharmacologic inhibition of α1- or α2-adrenergic receptors did not interfere in the RET-induced atrophy of the ileal epithelial layer (Fig. 6B), metyrosine that inhibits the enzymatic capacity of TH to transform L-tyrosine in L-DOPA, β1- or β2-specific or nonspecific pan-β-adrenoreceptor blockade, as well as reserpine, which irreversibly inhibits the vesicular monoamine transporter of catecholamines involved in their release in the synaptic cleft, all prevented RET-induced reduction of the villus/crypt height ratios (Fig. 6B). Accordingly, the use of the β-adrenergic receptor agonist clenbuterol tended to exacerbate the cancer-associated ileopathy (Fig. 6B). In contrast, the anticholinergic agent atropine, which competitively antagonizes the actions of acetylcholine and other muscarinic agonists on all muscarinic receptors within exocrine glands, ganglia, and intramural neurons, could not reverse the effects of tumor progression on the

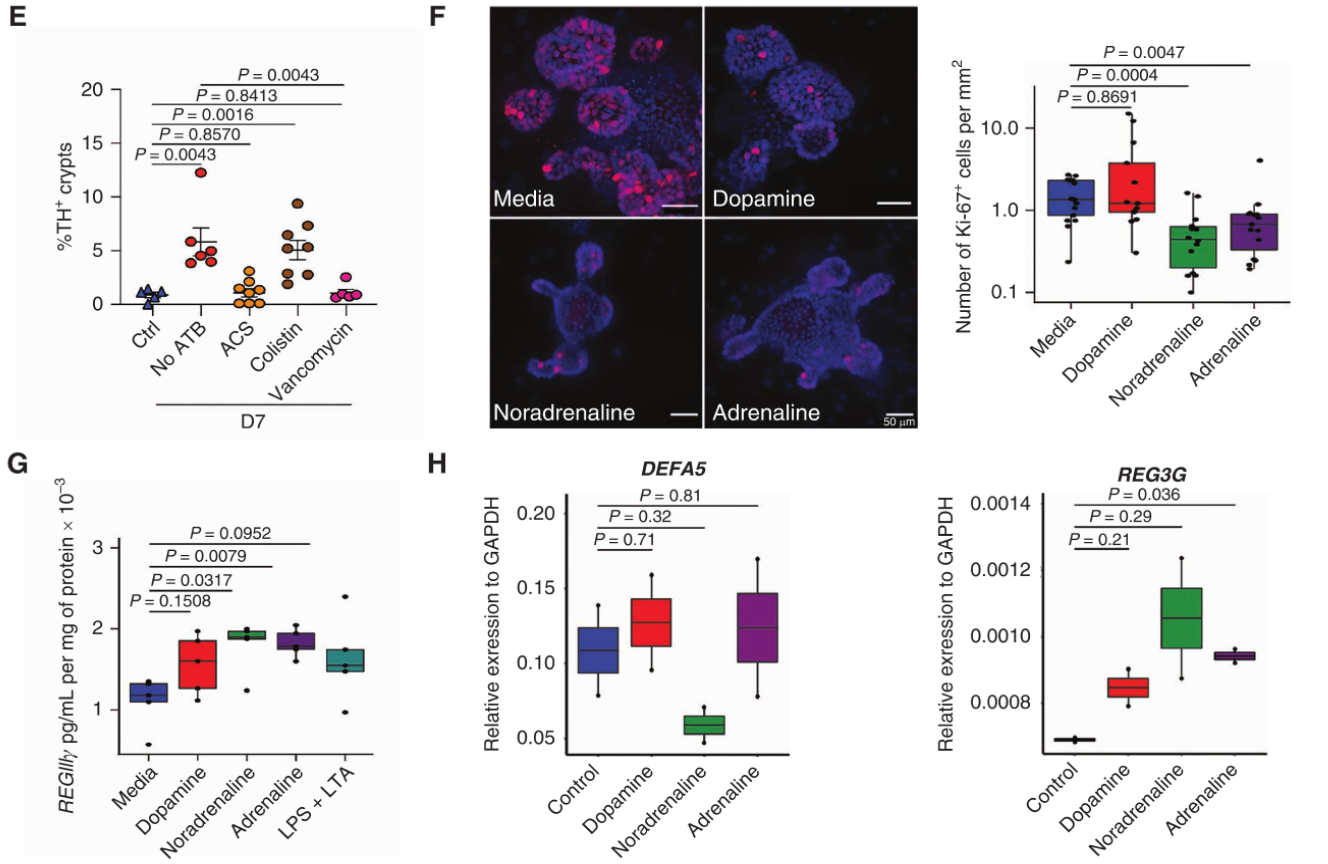

Figure 5. ***(Continued)*** **E,** IHC staining specific for TH expression in ileal crypts of RET tumor bearers that were treated with various regimens of antibiotics during 7 days. The graphs depict a pool of two independent experiments comprising 5–6 mice/group. Mann–Whitney test was used for comparison versus control group. **F–H,** Mouse (**F–G**) and human (**H**) 3-D ileal crypt stem cell–derived enteroids stimulated with catecholamines (**F–H**) or LPS + LTA (**F–G**) 24 hours at day 5 after enteroid dissociation (**F–G**) or for three days (**H**). **F,** z-stacks projection of confocal microscopy images of immunofluorescent staining of Ki-67 and nuclei (with DAPI) in mouse intestinal organoids and ELISA assessment of REG3γ protein normalized to total proteins in the enteroid lysates (**G**). A representative experiment showing raw data for each individual well (out of two yielding similar results) is depicted. **H,** PCR determination of the expression levels of antimicrobial peptide and defensin gene products in human enteroids exposed to various catecholamines. Normalized transcriptional expression of the *REG3*G gene (and *DEFA5*) in human ileal organoids that were differentiated for 4 days and then stimulated with 100 µmol/L adrenaline, noradrenaline, or dopamine for 3 days ($n = 2$). Similar conclusions were drawn when stimulating the organoids for 24 hours ($n = 2$). Of note, expression levels of the *DEFA5* gene (left) did not change in similar conditions. Mann–Whitney test was used for comparison versus control group.

ileum (Fig. 6C). Similarly, the steroidal antiprogestogen mifepristone, which prevents binding of cortisol to the glucocorticoid receptor, did not interfere in the tumor-induced ileopathy (Fig. 6C). Prophylactic intake of the β1/β2 adrenergic receptor antagonist propranolol could prevent crypt degranulation and apoptosis, as well as the accumulation of CgA^+ cells (Fig. 6D), when administered at the time of tumor implantation. The pharmacologic inhibition of β-adrenoreceptors phenocopied the effects of the *Adrb2* gene deficiency. The epithelial atrophy could no longer be observed in *Adrb2*$^{-/+}$ or *Adrb2*$^{-/-}$ mice (Fig. 6E). The RET-induced reduction of the villous microvascular thickness that may be related to vasoconstriction was also dependent on the sympathetic tonus (Fig. 6F). However, the pan-β-adrenoreceptor blockade failed to significantly interfere in cancer-induced deviations of the taxonomic composition of the microbiota. Although propranolol and metoprolol could somehow prevent the imbalance between *Ruminococcaceae* and *Lactobacillaceae* family members induced by RET implantation at day 8, the β-diversity of the whole intestinal ecosystem was not different in RET tumor bearers treated or not with propranolol (Supplementary Fig. S6A and S6B).

Based on our rationale and former work showing that pan-β blockers affect the immune system and benefit patients and mice bearing melanoma treated with immunomodulators such as rIL2, anti–PD-1 antibodies, or combination-based therapies (21), we addressed whether β-blockade could interfere in the tumor growth kinetics alone or combined with anti–PD-1 antibodies (Supplementary Fig. S6C). The pan-β-blocker propranolol but neither the β2 adrenergic receptor antagonist ICI118551 nor the β2 adrenergic receptor agonist clenbuterol could slow RET and MCA205 outgrowth (Fig. 6G and H), eventually boosting the effects of PD-1 and CTLA4 co-blockade (Supplementary Fig. S6C).

Altogether, cancer-induced ileopathy is a corollary syndrome of distinct malignancies, compromising the epithelial barrier and immune fitness, eventually contributing to cancer progression.

The Gut Oncomicrobiome Signature of Patients with Cancer

We next addressed whether cancer-associated ileopathy has clinical significance in humans. Pioneering reports dating

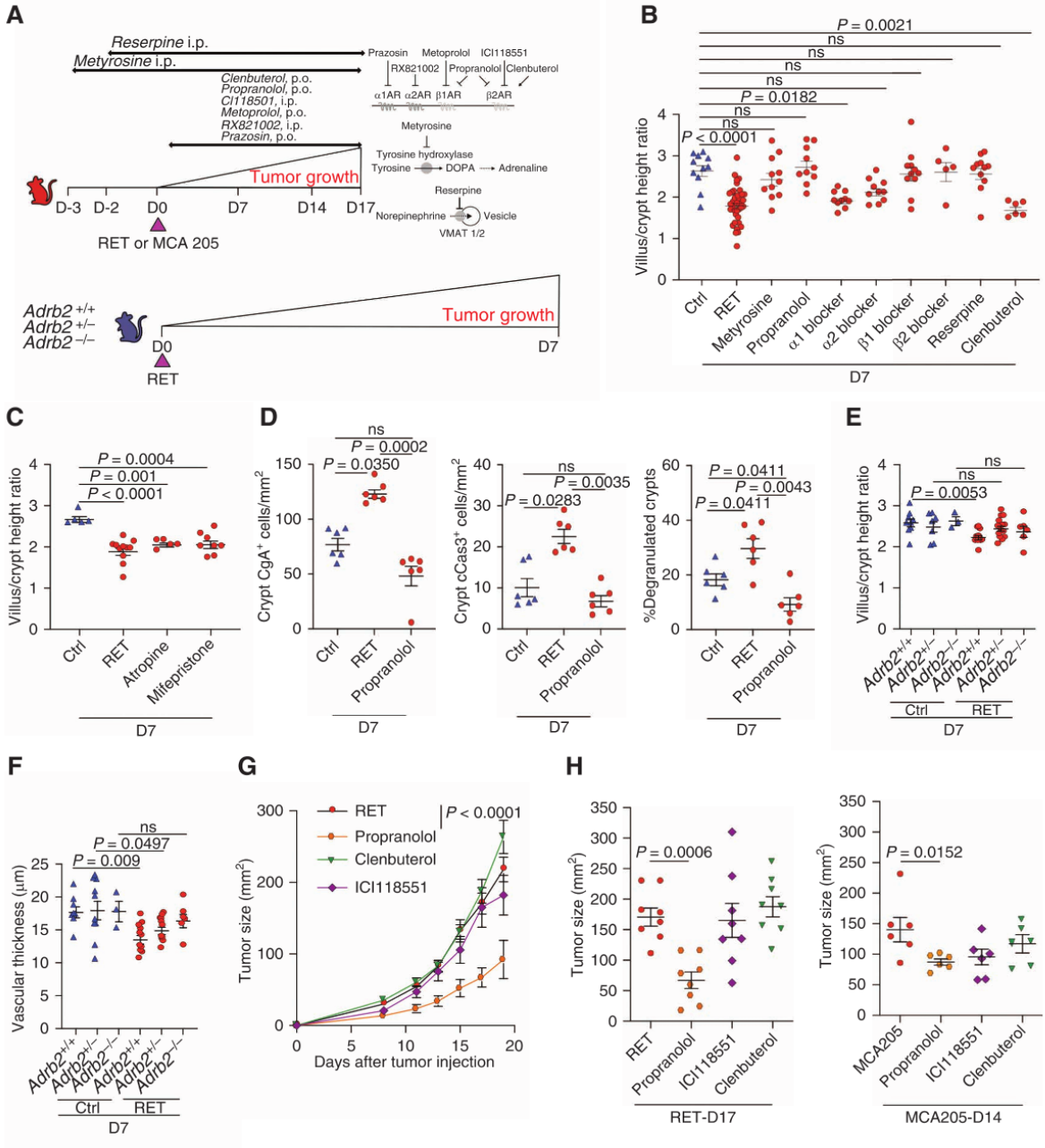

Figure 6. β-Adrenoreceptor signaling controls cancer-induced ileal atrophy. **A,** Graphical scheme of molecular pathways relevant for the catecholamine release or adrenergic receptor signaling and pharmacologic inhibitors (or agonist) used in the following experiments and experimental setting to investigate the effects of various pharmacologic inhibitors or agonist (clenbuterol) of the sympathetic nervous system on RET or MCA205 tumor growth kinetics. **B** and **C,** Villus/crypt height ratio in RET melanoma bearers treated with various pharmacologic inhibitors or agonist (clenbuterol) of the sympathetic nervous system (**B**) or the glucocorticoid or muscarinic receptors (**C**) during 7 days from at least two independent concatenated experiments comprising 5–6 animals/group, each dot representing one ileum. ANOVA statistical analyses (Kruskal–Wallis test) were used for multiple comparisons. Numerical *P* values are indicated. **D,** Modulation of ileal crypt EEC hyperplasia (left), cell apoptosis (middle), and degranulation (right) with propranolol at day 7 in RET-inoculated animals. A representative experiment out of two is depicted, each dot representing one distal ileum. ANOVA statistical analyses (Kruskal–Wallis test) were used for multiple comparisons. Numerical *P* values are indicated. **E** and **F,** The same as in **B**, but using *Adrb2* gene–deficient mice (homozygous or heterozygous littermates) to enumerate villus/crypt height ratio (**E**) and the villous microvasculature thickness at day 7 (**F**). ANOVA statistical analyses (Kruskal–Wallis test) were used for multiple comparisons. Numerical *P* values are indicated. **G** and **H,** Effects of various pharmacologic inhibitors or agonist (clenbuterol) of the sympathetic nervous system on RET or MCA205 tumor growth kinetics, longitudinal RET melanoma growth (**G**, survival curves were estimated using the Kaplan–Meier product limit method), and cross-sectional assessment at sacrifice for RET (**H**, left) and MCA205 (**H**, right) depicted by means ± SEM of tumor sizes, over time or at sacrifice for 6–8 animals/group. Mann–Whitney test was used for comparison versus control group.

from the 1960s already described morphologic abnormalities observed in ileal mucosae of patients diagnosed with advanced malignancies, but this contention was disputed as "spurious" due to numerous confounding factors such as performance status alterations and cachexia that blurred the interpretation of this corollary disease (22–25). Owing to the regulatory constraints limiting endoscopy/biopsy of the distal ileal epithelium in patients recently diagnosed with extraintestinal malignancy, we limited our study to patients diagnosed with proximal colon cancers who underwent surgical resection of terminal ileum.

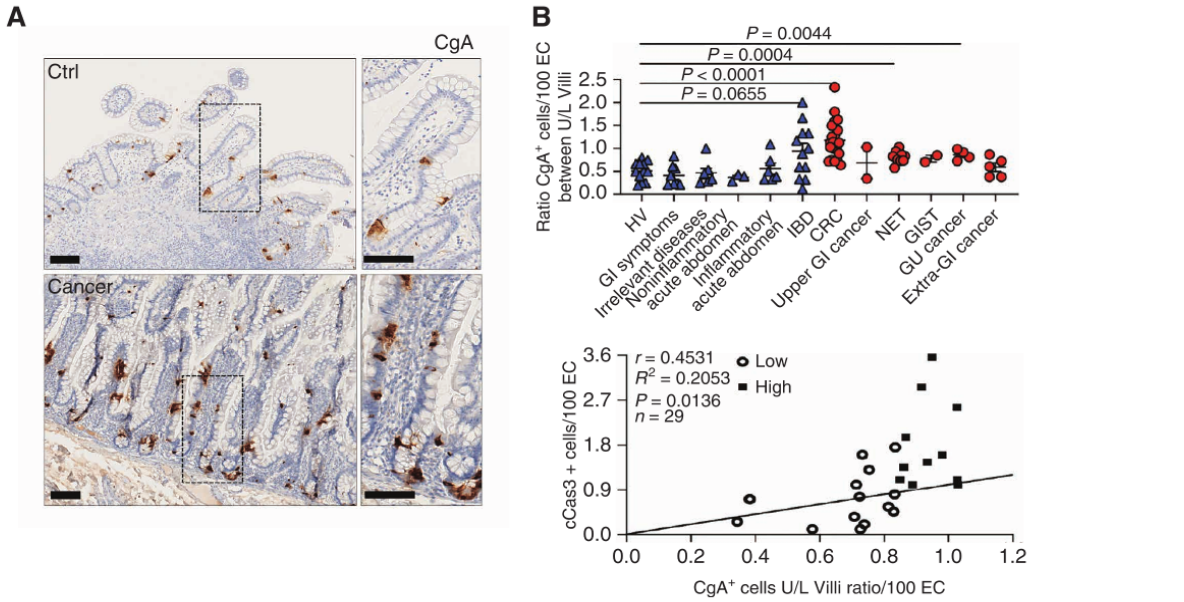

Figure 7. Gut oncomicrobiome MG-based signature across 8 different human malignancies. **A** and **B,** IHC assessment of CgA$^+$ and cleaved caspase-3$^+$ cells in the ileum of "healthy" cancer-free volunteers (HV), patients suffering from colorectal cancers (CRC) or cancers distant from the digestive tract (melanoma, ovarian cancer, kidney or bladder cancer, and Burkitt lymphoma) or inflammatory bowel disease (IBD) or irrelevant diseases [tumor-free individuals without gastrointestinal (GI) tract–related disorders]. Quantification of CgA (top) and Spearman correlation with cleaved caspase-3 (bottom) at diagnosis (refer to Supplementary Table S1 for description of patient characteristics), each dot representing one patient's sample. Numerical *P* values are indicated for Mann–Whitney test versus HV. EC, epithelial cells; GIST, gastrointestinal sarcoma; NET, neuroendocrine tumors; GU, genitourinary cancer. A representative micrograph picture of the ectopic hyperplasia of EEC (**A**) and enumeration (**B**, top) of CgA$^+$ cells in the upper (U) and lower (L) part of the villus in five independent fields/individual, each dot representing the ratio U/L between these two values in one ileum sample (biopsy or surgical resection; **B**). Scale bar, 100 μm. (*continued on following page*)

As described in mice, two independent pathologists observed increased proportions of CgA$^+$ EECs in the crypts, often harboring an ectopic distribution reaching the villi tips in patients diagnosed with colon cancer, genitourinary tumors, or neuroendocrine tumors compared with cancer-free individuals (Fig. 7A and B), whereas Paneth cell numbers did not differ (Supplementary Fig. S7A). This EEC accumulation did not appear to be cancer-specific and could be observed in patients suffering from inflammatory bowel disease (Fig. 7B; Supplementary Table S1). Moreover, as seen in tumor-bearing mice, the ectopic accumulation of EEC at the top of the villi correlated with ileal crypt apoptosis in patients (Fig. 7B, bottom). However, in contrast to mice, there were no abnormalities in the proliferative capacities of ileal enterocytes in cancer bearers (Supplementary Fig. S7B). As described in mice, 145 patients with advanced-stage cancer also harbored the specific serum hallmarks of gut permeability (such as soluble CD14 and ST2) compared with healthy individuals (Fig. 7C; Supplementary Table S2).

Based on the premise that cancer might be associated with a corollary gut dysbiosis, we prospectively carried out a shotgun MG-based analysis of fecal material harvested from the largest series of patients with cancer ever reported so far. In a prospective cohort of 1,426 patients with cancer across 8 different malignancies and disease staging, we collected the stools from patients harboring kidney cancer ($n = 69$), breast cancer ($n = 83$), lung cancers ($n = 368$), melanoma ($n = 108$), prostate cancers ($n = 47$), ovarian cancers ($n = 29$), and chronic myelomonocytic leukemia ($n = 17$). These samples were integrated to 705 colon cancers from the publicly available database (26). This collection of cancer metagenomes was compared in terms of species-level taxonomic profiles with 5,570 healthy individuals. Baseline characteristics of patients with cancer in each cohort are presented in Supplementary Table S3. Based on prior studies demonstrating a higher diversity of the gut microbiome in patients with melanoma responding to anti–PD-1 blockade (2), we first compared the alpha diversity in cancer versus cancer-free individuals, and observed no significant differences across multiple diversity metrics (Shannon index; Supplementary Fig. S7C). We then performed PCoA for microbial β-diversity, which provides a measure of the overall relatedness between samples. Significant differences separated bacterial species from feces of individuals with cancer versus those without cancer ($P < 0.01$; Fig. 7D). Using linear discriminant analysis of effect size (LEfSe; ref. 27), coupled to a pairwise comparison of relative taxonomic abundances (for species having a prevalence equal to or greater than 5%) using bootstrapping of two-tailed Mann–Whitney *U* tests (with 1,000 permutations and correction for continuity and ties), we concluded that selected bacterial taxa [$N = 25$; such as Prevotella genus (*P. copri*, *P. stercorea*, and *P. sp CAG520*), Lachnospiraceae family members (*Eubacterium hallii*, *E. ventriosum*, *E. rectale*, *Eubacterium sp CAG 274*, *D. longicatena*, *Roseburia sp CAG 471*, *R. faecis*, *C. comes*, and *Anaerostipes hadrus*), *Actinobacteriaceae* (*Collinsella aerofaciens*, *Bifidobacterium adolescentis*, *B. pseudocatenulatum*, and *Aeriscardovia aeriphila*), *Lactobacillaceae* (*L. rogosae* and *L. ruminis*); Fig. 7E] were overrepresented in healthy individuals. Conversely, distinct bacterial species were overrepresented in patients with cancer across 6 of 8 cancer types, such as 10 Gram-positive commensals, belonging to the *Clostridia* class or Clostridiales order (such as *Clostridium boltae*, *C. citroniae*, *C. clostridioforme*, *C. asparagiforme*, *C. lavalense*, *C. sp CAG242*, *C. symbosium*, and *Ruthenibacterium lactatiformans*), gamma- and delta-proteobacteria (*Bilophila wadworthia* and *Hafnia alvei*),

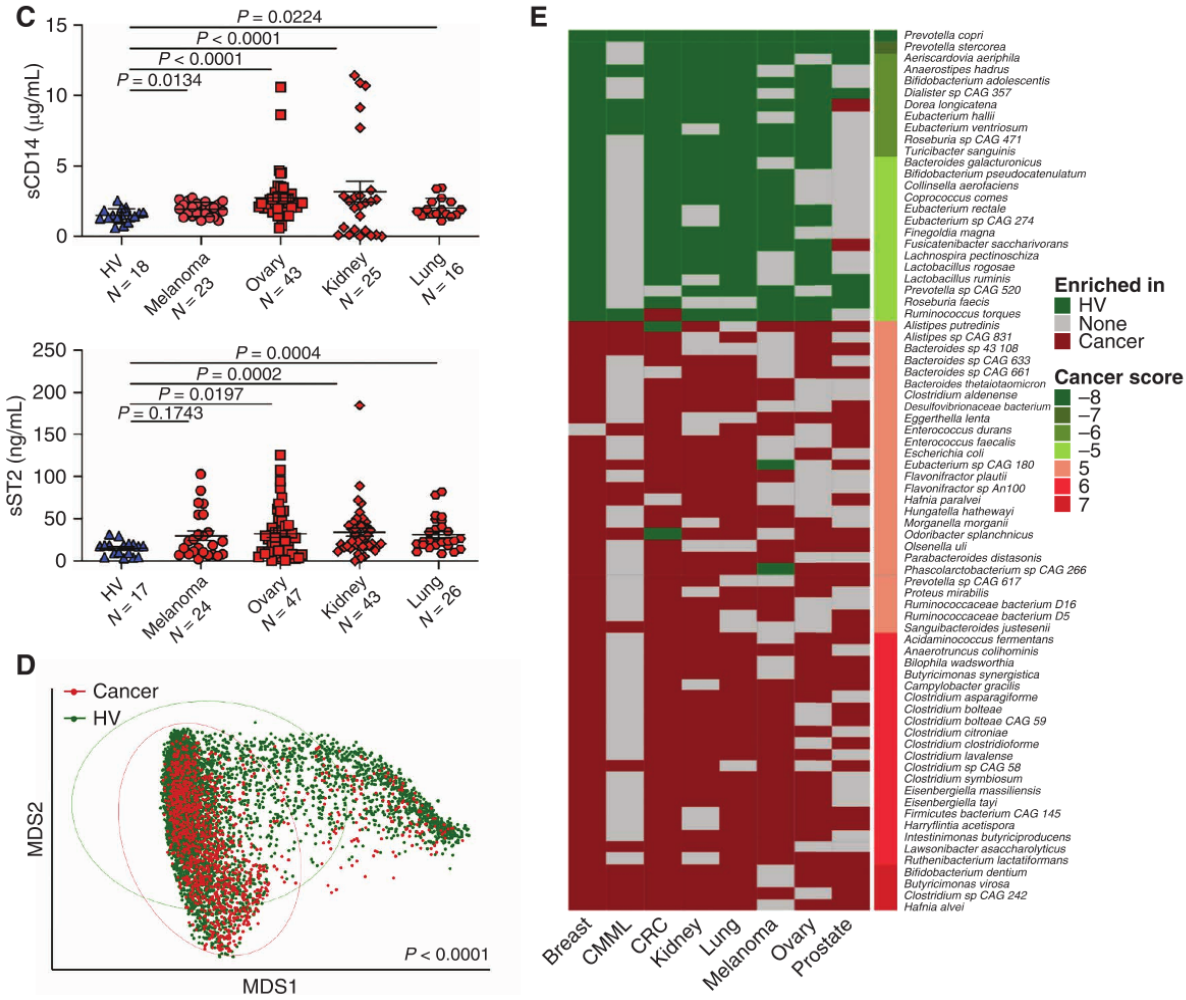

Figure 7. ***(Continued)*** **C,** Quantification of CD14 (top) and soluble ST2 (bottom) in the serum of healthy volunteers (HV) and patients with cancer (melanoma, ovarian cancer, kidney cancer, and non–small lung cell carcinoma) at diagnosis (refer to Supplementary Table S1 for description of patient characteristics), each dot representing one patient's sample. Numerical *P* values are indicated for Mann–Whitney test versus HV. Statistical analyses were performed comparing HV and each cancer histologic type using Student *t* test. **D,** Shotgun MG-based analysis of fecal material harvested from 1,637 patients with cancer (refer to Supplementary Table S2 for description of patient characteristics) and 5,570 HVs. Pairwise comparison on relative taxonomic abundances highlighting species that are over- or underrepresented in multiple cancer types. **E,** The heat map shows the most relevant species as those significant in at least five out of eight cancer categories.

Bifidobacterium dentium, and *Butyricimonas virosa*, as described in rodents and reported in patients with kidney cancer who took antibiotics or failed to respond to immune checkpoint inhibitors (ref. 28; Fig. 7E). We conclude about the prominence of a gut oncomicrobiome fingerprint shared across several tumor types and mammalian species (rodents and humans) where commensals associated with ATB-induced dysbiosis and immunoresistance (mostly Gram-positive bacteria belonging to the Clostridiales order or Proteobacteria) take over beneficial microbes associated with a healthy status.

Altogether, we show a protracted intestinal dysbiosis, most likely associated with stress-induced ileopathy, as a new pathologic feature of cancer progression independent of cachexia in patients with cancer and rodents.

DISCUSSION

Our findings highlight for the first time ileal epithelial dysfunction as a corollary to carcinogenesis initiation that contributes to its pathogenesis and causes a protracted gut dysbiosis. First, the pathologic hallmarks of cancer-associated ileopathy, characterized by mucosal atrophy (abrasion of villi tips), are unexpected in that they occurred rapidly after tumor implantation and are orchestrated in a coordinated manner. This pathogenesis involves defects in endoplasmic reticulum (ER) stress response and autophagy activation, as well as apoptosis of crypt cells accompanied by decreased proliferation in the maturation zone, loss of lymphocytes, granulocytes, and eosinophils, Paneth cell degranulation (with increased REG3γ/defensins ratios), and EEC accumulation in the crypts with ectopic distribution to the villus tip. They are more pronounced in the terminal ileum, reaching the proximal ileum with a short lag, but spared the upper small and large intestine. Following these criteria, the hallmark characteristics of the cancer-associated ileopathy differ from bona fide gut disorders characterized by inflammation or immune-related pathologies or Th2-associated infectious diseases (29–31). However, they are reminiscent of the "cancer enteropathy" first

observed by physicians in 1965 (22–24). Authors described frequent partial (in 10%–29% cases) or subtotal (1%–2% cases) villus atrophy of duodenum, jejunum, or ileum in patients with cancer independent of metastases, treatments, interval to death, or steatorrhoeae, but proportional to duration of the malignancy and weight loss (23, 24).

In mice, the hallmark characteristics of the cancer-associated ileopathy were transient, starting at day 3, peaking at day 8, and resolving at day 12 (when tumors reached a surface of about 20 mm^2), followed by a long-lasting intestinal dysbiosis where Gram-positive bacteria (mostly belonging to the Clostridiales order) prevail in the ecosystem. Owing to its rapid onset, cancer-associated ileopathy did not coincide with body-weight loss nor systemic inflammation due to cachexia. However, it shared with cachexia-associated microbial dysbiosis the relative loss of Lactobacillus genus, the increased gut permeability, and endotoxemia (25, 32, 33). We excluded a role for mucosal T-cell activation in this process (because they were reduced within and outside blood vessels, maybe due to vasoconstriction), as well as a dysregulation of tight junctions, but uncovered a biologically significant imbalance between sympathetic and parasympathetic signals in specific areas of the mucosa. ChAT-producing cells were reduced in the stroma, whereas tyrosine hydroxylase–expressing cells accumulated in the crypts to potentially release biogenic amines (such as epinephrine) that may be, at least in part, a source of the villous microvascular constriction and ileal damage (reduced Ki-67 and increased REG3γ secretion). EEC and Paneth cells were previously reported to express TH, either constitutively for the former ones, or after kidney injury for the latter ones (13, 19, 34). Hence, although the mechanisms by which ileopathy is triggered or maintained during cancer progression remain largely unclear, our findings allow us to speculate that the deviated repertoire of the gut microbiota with the predominance of *Clostridium spp.* may induce EEC production of biogenic amines that in turn signal in and stimulate Paneth cell neighbors to produce and release antimicrobial peptides to control ileal dysbiosis.

Blockade of β-adrenoreceptors limited the growth of extra-intestinal tumors, mostly in those generating the cancer enteropathy. In that regard, Stanley and colleagues showed that ischemic brain injuries caused gut barrier dysfunction and increased permeability, allowing the translocation of ileal bacteria to peripheral organs, paving the way to Gram-positive lung infections. These authors unveiled a biologically significant imbalance between adrenergic and cholinergic signaling within the submucosal plexus in the ileum post-stroke. Indeed, reduction in cholinergic signaling stimulated the proinflammatory immune response (35), whereas its activation prevented the brain injury–induced increase in both intestinal and cerebral vascular permeability (36, 37). Adrenergic-mediated systemic immunosuppression was shown to be beneficial after stroke (38). The pan-β-blocker propranolol could decrease gut permeability post-stroke and reduce bacterial translocation to the lung parenchyma. Moreover, neutralizing β3 adrenoreceptors after stroke could block the bone marrow exodus of inflammatory monocytes (39), which can also be a source of biogenic amines, and contribute to a feedback-positive loop of systemic inflammation (40). Of note, our data indicate that there was no myeloid cell recruitment in ilea post–tumor implantation. Catecholamines mediate numerous functions in the intestine. At the level of epithelial dynamics, noradrenaline release from the sympathetic nervous system appears to stimulate crypt cell proliferation in both the small and large intestines through signaling via α2 adrenoceptors (41). Conversely and in accordance with our findings, adrenaline inhibits cell division in both normal and neoplastic intestinal epithelial cells (IEC) through β-adrenoreceptors (42).

The intestinal immune and nervous systems are intertwined, sensing and integrating luminal cues to regulate motility. The involvement of catecholaminergic neurons in anti-inflammatory responses has been demonstrated in different tissues and is attributed to the broad sympathetic innervation in peripheral lymph nodes associated with expression of β2-adrenergic receptors in immune cells. Recent evidence suggested that intestinal resident macrophage populations play a role in the normal functioning of enteric neurons in homeostatic conditions (43, 44). Specifically, muscularis macrophages (MM), located within and surrounding the myenteric plexus, were shown to regulate the activity of enteric neurons and peristalsis via secretion of bone morphogenetic protein 2 in a microbiota-dependent manner (44). Moreover, MMs displayed a tissue-protective gene-expression profile, a signature that was enhanced following enteric infection, and involved β2-adrenergic receptor signaling (45). While not affecting pathogen load, β-blockade by salbutamol protected mice from enteric nerve loss through a mechanism involving arginase 1 and polyamines (46).

The circuitry connecting luminal sensing to enteric neurons remains largely unknown (47, 48). Recent work directly connected the microbiota to transcription factors in enteric neurons (47, 49) regulating their function. Some lines of evidence suggest that sensing of luminal pathogens, or associated changes in the bowel environment, could be mediated by an intermediate cell type, the EEC (50) or mucosal-associated pain sensory afferents (51), both with the capacity to affect enteric neuron survival and/or activation. Although EECs can synapse with vagal neurons to transduce gut luminal signals in milliseconds by using glutamate as a neurotransmitter, our data suggest that EEC may also express TH and produce catecholamines, as already reported (13).

Interestingly, not all tumorigenic processes trigger this ileopathy. Heterotopic (MC38) or orthotopic (RENCA, fibrosarcoma, RET melanoma) cancers could do so, but even within the same histology (i.e., melanoma), we observed major differences between cell types (B16F10 and RET). It was not a peculiarity of mouse genetic background because RENCA, syngeneic of BALB/c, and all the others (syngeneic of C57BL/6) could elicit ileal dysfunctions. Our findings strongly suggest that soluble products secreted from cancer cells may be transferred to and sensed by distinct epithelial and/or neuronal and/or immune components of the ileal mucosae. Previous work documented that extracellular vesicles from p53-deficient (but not proficient) cancer cells could shuttle tumor miRNA capable of reprogramming the transcriptional profile of existing nerves, resulting in axonal sprouting and emergence of adrenergic nerves indispensable for tumor development (52). In fact, the biological significance of the sympathetic nervous system in tumor progression has already been reported in prostate

and head and neck tumors (52, 53). However, our data do not support this scenario, as we failed to observe any exacerbated innervation of subcutaneous tumors and differences between tumors associated or not with enteropathy. Plasma proteomics and metabolomics as well as bone marrow chimeras could help disentangle stromal versus tumoral cues inducing stress ileopathy.

Our findings rather support the notion that the sympathetic nervous system (or the imbalance within the autonomous nervous system circuitries) indirectly affects natural tumor immunosurveillance. Indeed, β-blockade boosted the efficacy of anti–PD-1 antibodies in MCA205 and RET tumor models. In fact, previous work has already reported that patients with melanoma or breast cancer who took pan-β-blockers presented a greater benefit to immunotherapy or chemotherapy, respectively, as a consequence of increased accumulation of tumor-infiltrating lymphocytes within the tumor microenvironment (21, 54). Indeed, intestinal dysbiosis favoring the dominance of short chain fatty acid–producing immunosuppressive bacteria and/or the translocation of *Lactobacilli* spp. endowed with tolerogenic properties may compromise several of the tumor immunosurveillance mechanisms (2, 8, 28).

Regardless of the precise molecular cues underlying the connections between cancer enteropathy and β2 adrenergic signaling, our data illustrate that the cancer-associated ileopathy is a debilitating corollary syndrome of the tumorigenic process, inducing a long-lasting dysbiosis perturbing the delicate host–tumor balance. Novel diagnosis tools and specific interceptive therapeutics are needed to interfere in this negative feedback loop.

METHODS

Cell Culture, Reagents, and Tumor Cell Lines

MC38, MCA-205, B16F10 (syngeneic from C57BL/6J mice), and 4T1 cell lines (syngeneic from BALB/c mice) were purchased from the American Type Culture Collection, whereas the AT3 breast cancer cell line (syngeneic from C57BL/6J mice) was kindly provided by Dr. Mark Smyth (QIMR Berghofer, Brisbane, Australia). The RET melanoma cell line, generated by transgenic expression of the *RET* proto-oncogene under the control of the metallothionein-1 promoter driving spontaneous melanogenesis, was provided by Viktor Umansky (DKFZ—German Cancer Research Center; syngeneic from C57BL/6J mice). The luciferase-transfected RENCA cell line (syngeneic for BALB/c mice) was provided by Transgene. Cells were cultured at 37°C with 5% CO_2 in RPMI 1640 containing 10% FCS, 2 mmol/L L-glutamine, 1% penicillin/streptomycin, and 1% sodium pyruvate and nonessential amino acids. All reagents were purchased from Gibco-Invitrogen. Dead RET cells were created by repeating freezing and thawing of the RET cell line three times continuously, and viability of the cell line was evaluated by the Vi-CELL Cell Viability Analyzer. Cell lines were regularly tested for *Mycoplasma* contamination and were not used after more than 10 passages.

Mice Experiments

Ethics, Guidelines, and Providers. All animal experiments were carried out in compliance with French and European laws and regulations. The local institutional animal ethics board and French Research Ministry approved all mouse experiments (permission numbers: 2020_035_25416). Experiments were performed in accordance with government and institutional guidelines and regulations. Female C57BL/6 mice were purchased from Harlan. Mice were used between 7 and 12 weeks of age. All mouse experiments were performed at the animal facility of Gustave Roussy Cancer Campus where animals were housed in specific pathogen-free conditions.

Subcutaneous Transplantable MCA-205 Sarcoma, MC38, B16F10, and RET Melanoma. Mice were implanted with 0.8×10^6 MCA-205 sarcoma, 1.0×10^6 MC38, 0.3×10^6 B16F10, or 0.5×10^6 live or dead RET melanoma, 0.5×10^6 AT3 breast cancer, and 0.3×10^6 4T1 cells subcutaneously. Tumor-inoculated mice were treated intraperitoneally when tumors reached a 20 to 40 mm^2 size with anti–PD-1 mAb (250 μg/mouse; clone RMP1-14 purchased from Bio X Cell), anti-CTLA4 (100 μg/mouse, clone 9D9 purchased from Bio X Cell) or isotype controls (clones 2A3 and MPC11, respectively) three times at three-day intervals. Tumor length and width were routinely monitored every three days by means of a caliper.

Pharmacologic Treatment

α- and β-Blockade. We conducted intraperitoneal (i.p.) injection of prazosin (purchased at the local pharmacy of Gustave Roussy) at a concentration of 1.5 mg/kg of mice twice a week for α1 blockade, RX821002 (Tocris) at a concentration of 10 mg/kg of mice daily for α2 blockade, metoprolol (purchased at the local pharmacy of Gustave Roussy or Sigma) at a concentration of 10 mg/kg of mice daily for β1 blockade, and ICI118551 (Tocris) at a concentration of 10 mg/kg of mice daily for β2 blockade. For pan-β-blocker or agonist experiments, mice were treated from the day of tumor inoculation with autoclaved drinking water containing propranolol (Sigma or purchased at the local pharmacy of Gustave Roussy) at a concentration of 0.5 mg/mL and filtered through a 0.22-μm membrane or clenbuterol (Sigma) at a concentration of 9 μg/mL, which was refreshed twice a week.

Catecholamine Depletion. Metyrosine (α-Methyl-D, L-p-tyrosine; CliniSciences) at a concentration of 60 mg/kg of mice was injected i.p. three days before and daily after tumor injection. Reserpine (Sigma) was injected i.p. 48 hours before tumor inoculation at a concentration of 5 mg/kg of mice.

Anticholinergic Agent and Steroidal Antiprogestogen. Atropine (purchased at the local pharmacy of Gustave Roussy or Sigma) and mifepristone (Sigma) at a concentration of 30 mg/kg and 4 mg/kg of mice, respectively, were injected i.p. daily.

The RENCA-luc Orthotopic Tumor Model. BALB/c mice were anesthetized with isoflurane. A lateral incision was made on the dorsolateral right flank of each mouse. 10^4 Renca-Luc cells resuspended in 30 μL PBS were injected into the subcapsular space of the right kidney. The skin incision was then closed with surgical clips. Tumor growth was monitored after 15 days of tumor injection using an IVIS Imaging System 50 Series (Analytic Jenap). At day 15, mice were euthanized to harvest small intestines and perform ileum Swiss roll.

Orthotopic Luciferase-Engineered TC1 Lung Cancer Model. TC1 cells stably expressing firefly luciferase (TC1-Luc, 4×10^5 in 100 μL PBS) were percutaneously injected into the right lung of wild-type C57BL/6 mice. Tumor incidence and development were regularly monitored by the *in vivo* photonic imaging of tumor cells' luciferase activity. In brief, mice received a percutaneous injection of luciferase substrate (Beetle Luciferin potassium salt, Promega) at a dose of 150 mg/kg, and 8 minutes after luciferin inoculation, photons were acquired on a Xenogen IVIS 50 bioluminescence *in vivo* imaging system (Caliper Life Sciences Inc.). Tumor-bearing mice were sacrificed at days 7, 14, and 21 after tumor injection.

TC1 Intravenous (IV) Model. To establish the non–small cell lung carcinoma IV model, TC1 cells stably expressing firefly luciferase (TC1-Luc, 5×10^5 in 100 μL PBS) were intravenously injected into wild-type C57BL/6 mice. Tumor incidence and development were regularly monitored by *in vivo* photonic imaging of tumor cells' luciferase

activity. In brief, mice received an i.p. injection of luciferase substrate (Beetle Luciferin potassium salt, Promega) at a dose of 150 mg/kg, and 8 minutes after luciferin inoculation, photons were acquired on a Xenogen IVIS 50 bioluminescence *in vivo* imaging system (Caliper Life Sciences Inc.). Two weeks after cell injection (day 14), tumor incidence in the lung was detected at an exposure time of four minutes. *In vivo* imaging was conducted every four to five days with an exposure time starting with four minutes, which was then gradually decreased to three, two, and one minute when photon saturation occurred. Tumor-bearing mice showing photon saturation within less than one minute of exposure were euthanized.

Antibiotic Treatments. Mice were treated with antibiotic solution containing ampicillin (1 mg/mL), streptomycin (5 mg/mL), and colistin (1 mg/mL; Sigma-Aldrich), or colistin alone (1 mg/mL), or vancomycin alone (0.25 mg/mL) added in autoclaved drinking water. Antibiotic solutions were refreshed and bottles were replaced three times a week.

Cohousing Experiments. The same number of RET-injected mice (C57BL/6J females) were cohoused as littermates with naïve (non–tumor-bearing) mice (C57BL/6J females) in the same cage from the day of tumor injection until sacrifice. As for methylcholanthrene-induced sarcoma, MCA inoculated and noninoculated mice were admixed in the same cage in a 1:1 ratio or left alone in separate cages. Groups of wild-type C57BL/6 mice were injected subcutaneously in the flank with 100 µg of 3-MCA in 0.10 mL of corn oil. Mice were monitored every 7 days for tumor development 90 to 100 days after 3-MCA treatment. Animals bearing nodules >0.5 cm^2 in area and demonstrating progressive growth were considered as "tumor" nodules, as previously described (12).

RNA Extraction and PCR to Determine Gene Expression

Lysis and extraction protocols were identical for all murine samples. Tumor or intestinal samples were snap-frozen in liquid nitrogen in RLT and buffer containing 0.1% β-mercaptoethanol. On the day of extraction, samples were thawed at 4°C and homogenized on a microtube homogenizer (Benchmark Scientific) in RNA-free glass bead tubes (Dutscher). Total RNA extraction and genomic DNA removal were performed with the RNeasy Mini Kit (Qiagen), following the manufacturer's recommendations. A maximum of 1 µg of RNA, measured by using a NanoDropTM Spectrophotometer (Thermo Fisher Scientific), was reverse-transcribed into cDNA with a mix composed of SuperScript III Reverse Transcriptase (Life Technologies), RNaseOUT Recombinant Ribonuclease Inhibitor (Life Technologies), Random primers (Promega), and Deoxynucleoside Triphosphate Set, PCR grade (Roche Diagnostics).

Quantitative Gene Expression Assay. Expressions of murine Ppia (Mm02342430_g1), Ang4 (Mm03647554_g1), Lyz2 (Mm01612741_m1), Reg3γ (Mm00441127_m1), α Defensin-5 (Mm00651548_g1), defensin β1 (Mm00432803_m1), IFNα1 (Mm03030145_gH), IFNβ1 (Mm00439552_s1), IFNλ2 (Mm04204157_gH), Th (Mm00447557_m1), ChAT (Mm01221880_m1), Adrb1 (Mm00431701_s1), and Adrb2 (Mm02524224_s1; all from Life Technologies) were analyzed with the TaqMan Gene-Expression Assay using the Universal Master Mix II on a StepOnePlus Real-Time PCR System (Life Technologies). Amplifications were carried out using the following ramping profile: 1 cycle at 95°C for 10 minutes, followed by 45 cycles of 95°C for 30 seconds, 60°C for 1 minute. Quantitative RT-PCR data were normalized to the expression levels of the housekeeping gene Ppia by means of the $2^{-\Delta C}{}_t$ method.

Pathologic Methods and Analyses

Animal Handling after Sacrifice to Investigate the Digestive Tract. Mice were sacrificed at various time points post–RET (or tumor) inoculation. The intestinal tissues including duodenum, jejunum, ileum, and colon were harvested, and the lumen was flushed with sterile PBS. Each intestinal segment was cut longitudinally, rolled, and fixed in 4% paraformaldehyde (PFA) overnight. After fixation, the intestine tissue was preserved in formalin-fixed, paraffin-embedded or optimum cutting temperature compound.

IHC of Murine Intestinal Tissues. For morphologic analysis, a hematoxylin, eosin, and saffron staining was used. For all biomarker staining, we used Bond Leïca automated immunostainer instruments. For the detection of cleaved caspase-3, Ki-67, TH, VAChT, and CD8, paraffin sections were processed for heat-induced antigen retrieval (either ER1 corresponding citrate buffer pH6 or ER2 corresponding EDTA buffer pH9) for 20 minutes at 100°. Slides were incubated with the antibody for one hour at room temperature. The antibodies used were as follows: cleaved caspase-3 (Cell Signaling Technology, D4W2Z, rabbit, 1:100, ER2), Ki-67 (Cell Signaling Technology, D3B5, rabbit, 1:500, ER2), TH (Millipore, polyclonal, rabbit, 1:300, ER1), VAChT (Synaptic Systems, polyclonal, rabbit, 1:500, ER2), and CD8 (Cell Signaling Technology, D4W2Z, rabbit, 1:400, ER2). The signal was revealed with the Rabbit HRP PowerVision Kit (Leïca Biosystems, #PV6119). The signals were detected with diaminobenzidine (DAB). For the detection of ZO1, CgA, and E-cadherin, paraffin sections were processed for heat-induced antigen retrieval (either ER1 or ER2) for 20 minutes at 100°. Slides were incubated with the antibody for 30 minutes at room temperature. The antibodies used were as follows: ZO1 (Abcam, EPR19945-224, rabbit, 1:1,000, ER2), CgA (Immunostar, 1317001, rabbit, 1:1,000, ER1), and E-cadherin (Cell Signaling Technology, 24E10, rabbit, 1:100, ER2). To reveal the signal, slides were incubated with Bond Polymer Refine Detection Kit (Leïca Biosystems, #DS9390) and red chromogen. For the detection of double markers CD4/FOXP3 simultaneously, antigen retrieval was performed by incubating slides in ER2 buffer (pH 9.0) for 20 minutes at 100°C. Then, the antibodies were successively incubated for one hour at room temperature and detected, respectively, by Bond Polymer Refine Red Detection (Leïca Biosystems, #DS9390) and by Bond Polymer Refine Detection Kit (Leïca Biosystems, #DS9800). The antibodies used were as follows: CD4 (Cell Signaling Technology, D7D2Z, rabbit, 1:50, ER2) and FOXP3 (Cell Signaling Technology, D608R, rabbit, 1:200, ER1). These slides were successively revealed by red chromogen (Leica Biosystems) and HIGHDEF Black HRP chromogen/substrate (Enzo Life Sciences, #ADI-950-171-0030). Finally, the sections were counterstained by hematoxylin (Leica Biosystems). For Alcian Blue special stain, slides were deparaffinized with xylene and rehydrated with alcohol and water. Then, slides were incubated with Alcian Blue solution pH2.5 for 45 minutes at room temperature. Without rinsing, slides were covered with sodium tetraborate solution. Finally, slides were rinsed in distilled water, dried, and mounted with xylene-based media. Images for analysis were acquired as whole slide images (WSI) with a slide scanner Zeiss Axio Scan.Z1 and Olympus VS120 whole-slide imaging system.

Measurement of Villus/Crypt Height Ratio. WSIs of longitudinal sections from adult mouse small intestine (duodenum, jejunum, and ileum) were generated. Five representative areas of distal ileum were randomly selected from each mouse. Measurements of villus and crypt height were performed using QuPath (55), when crypt-villus units were well oriented. The ratio of villus height/crypt height was calculated based on the measurements of each crypt-villus unit. Tangentially cut or less than 3–5 not well-oriented villi or crypts were excluded from the analysis.

Analysis of IHC Biomarkers

Biomarkers in Whole Tissues. QuPath software was used (55). Regions of interest (ROI) were defined first by "Simple tissue detection" function and modified by hand in each WSI to quantify biomarker-positive cells, and "Positive cell detection" or "Object classification" functions were used for detection of Ki-67, CD4/FOXP3, and goblet cells, whereas other biomarkers such as cleaved caspase-3,

CgA, TH, CD8, and GR1 were quantified manually. To quantify biomarker-positive areas such as ZO1, E-cadherin, and VAChT, "Pixel classification" function was used, and the DAB$^+$ area was considered as a biomarker-positive area. Artifacts and other nonspecific structures stained by the biomarkers were manually excluded.

Whole-Mount Immunostaining and Clearing Procedure. Tissue samples were immunostained and cleared following the iDISCO$^+$ protocol. Briefly, samples were dehydrated using graded series of methanol solution and then bleached in methanol/5% hydrogen peroxide overnight at 4°C. Samples were rehydrated using graded series of methanol solution, permeabilized for two days at 37°C and incubated in blocking buffer: PTwH (0.2% Tween-20, 10 mg/L heparin in PBS), 5% DMSO, and 3% donkey serum for three days at 37°C. Tissues were incubated with primary antibodies at 37°C for one week, washed in PTwH, and incubated with secondary antibodies for two to three days. The antibodies used are as follows: rat anti-panendothelial cell antigen monoclonal antibody, unconjugated, clone MECA-32 (rat, 1:10, catalog no. 550563, RRID:AB_393754, BD Pharmingen), anti–tyrosine hydroxylase antibody (rabbit, 1:200, catalog no. AB152, RRID:AB_390204, Merck Millipore), anti-VaChT antibody (rabbit, 1:250, catalog no. 139 103, RRID:AB_887864, Synaptic Systems), Cy3-AffiniPure Donkey Anti-Rabbit IgG (H + L) antibody (Donkey, 1:500, catalog no. 711-165-152 RRID:AB_2307443, Jackson ImmunoResearch Labs), Alexa Fluor 647-AffiniPure Donkey Anti-Rat IgG (R + L) antibody (Donkey, 1:500, catalog no. 712-605-153 RRID:AB_2340694, Jackson ImmunoResearch Labs). Samples were washed in PTwH, dehydrated in graded methanol series, and equilibrated in 66% dichloromethane/33% methanol overnight. Delipidation was completed by immersion in 100% dichloromethane for 20 minutes. Finally, samples were immersed in dibenzyl ether to homogenize the refractive indices between the tissue and the imaging medium.

LSFM and Image Processing. Cleared samples were imaged at 0.63× zoom on a light-sheet fluorescence microscope (LSFM; Ultramicroscope II, LaVision Biotec) using Imspector Microscope controller software (Version 5.1.328, LaVision Biotec). Stack images were converted to Imaris files (.ims) using Imaris File Converter and opened with Imaris ×64 software (version 9.6; Bitplane) to obtain 3-D volume images. 3-D pictures were generated using the "snapshot" tool.

Biomarkers in Villi and Crypts. To calculate the cell density of biomarkers such as cleaved caspase-3 or CgA only in villi or crypts, areas of murine villi and crypts were identified by a deep learning–based method. Briefly, WSIs were cropped into 256 × 256 pixel tiles. Blank tiles and tiles with only debris or uninterpretable pieces of tissue were excluded. The neural network trained by pathologists (S. Yonekura and K. Ueda) performed the semantic segmentation of villi, crypts, LP in murine ileum and colon using Python library "Segmentation model."

Quantification of ChAT$^+$ or VaChT$^+$ Areas in Mucosa and Submucosa of murine ileum. Mice were implanted with 0.5×10^6 RET melanoma cells subcutaneously and sacrificed at day 3. A Swiss-roll tissue of ileum was collected and fixed, and the expression of VAChT was revealed by the IHC using DAB. Images displayed in the figures were acquired as WSIs with a digital slide scanner Olympus VS120. Image analysis was performed using QuPath (20). Briefly, the VAChT$^+$ area was identified by detecting the percentage of DAB$^+$ area within five representative (1.0 mm^2) manually annotated regions, corresponding to the mucosa and submucosa of the ileum, randomly selected for each mouse. Only nerve fibers were quantified, excluding the submucosal plexus.

Quantification of ChAT$^+$ Neurons in Myenteric Plexus. Distal ileum segments were fixed in 0.1 mol/L PBS containing 4% PFA at room temperature for three hours. Whole mounts of longitudinal muscle and myenteric plexus were obtained by microdissection and were permeabilized with PBS containing 4% horse serum (HS) and 0.5% Triton X-100 for one hour at room temperature. Tissues were then incubated with the following primary antibodies sequentially: rabbit anti-ChAT [gift from Prof. Dr. M. Shemann (TUM School of Life Sciences, Technical University of Munich, Freising, Germany), 1/1,000] for 72 hours, and human anti-neuronal marker (gift from CHU Nantes, 1/500) overnight, both containing 4% HS, 0.5% Triton X-100, and 0.02% sodium azide at room temperature. After washing, tissues were incubated for two hours at room temperature with the appropriate secondary antibodies and mounted with Pro-Long Gold Antifade Reagents (Thermo Fisher Scientific). A minimum of 20 ganglia per tissue (animals) was analyzed using an Olympus BX microscope.

Quantification of Immunofluorescence ChAT$^+$ Areas in Mucosa and Submucosa of Murine Ileum. ChAT-GFP transgenic mice were implanted with 0.5×10^6 RET melanoma cells subcutaneously and sacrificed at day 7. A Swiss-roll tissue of distal ileum was collected, fixed, and counterstained with DAPI for the nucleus. Images displayed in the figures were acquired as WSIs with a digital slide scanner Olympus VS120. Image analysis of ChAT$^+$ was performed using QuPath (20). Briefly, the ChAT$^+$ area was identified by detecting the percentage of the GFP$^+$ area within two to five representative (1.0 mm^2) manually annotated regions, corresponding to well-oriented mucosa and submucosa of the ileum, randomly selected from two to four different sections of the ileum from each mouse. Out-of-focus and not well-oriented areas were excluded from the analysis. Areas of ChAT$^+$ cells in the villi, crypts, or stroma (vessels/immune cells) were excluded from ChAT$^+$ nerve fibers area, but were counted separately for each mouse. Cases with less than 30 villi evaluated were excluded from the final analysis.

Quantification of CD8$^+$ Cells in the Ileum. WSIs were used to calculate CD8$^+$ cell density with QuPath. Five to eight representative regions (1.0 mm^2), randomly selected, were evaluated in the distal ileum of each mouse. CD8$^+$ cells were manually counted as intra- or extravascular, according to their location in well-oriented villi. Cases with fewer than 30 villi evaluated were excluded from the final analysis.

Quantification of GR1$^+$ Cells in the Ileum. WSIs were used to calculate GR1$^+$ cell density with QuPath. Due to the low number of cells present in the sample, GR1$^+$ cells were counted in the entire distal segment of the ileum, considering the presence of GR1$^+$ cells in the LP of the villi, among the crypts or total. Total length was determined for the segment of distal ileum of each mouse in order to define a normalized count of GR1$^+$ cells/mm.

Single-Cell RNA Sequencing

Ileum samples from C57BL/6 mice with and without RET melanoma were collected, and fat tissue, Peyer's patches, and feces were removed. Intestines were cut longitudinally, rolled up, and then cut transversally into small pieces into a tube. Pieces were transferred into a new 50-mL tube with 20 mL of IEC medium containing PBS, 5% FCS, 5 mmol/L EDTA, and 1 mmol/L DTT. Tubes were vortexed and shaken at 37°C for 20 minutes. Cell suspensions were filtered with a 40-µm cell strainer into a new tube, centrifuged, resuspended in a solution of PBS 1× (without EDTA and magnesium) containing 0.04% de BSA (400 µg/mL), and counted. Cell suspensions were stored in LoBind tubes at a concentration of 1.0×10^6 cellules/mL and kept on ice until use. Single-cell suspensions were loaded onto a chromium single-cell chip (10X Genomics) according to the manufacturer's instructions for coencapsulation with barcoded gel beads at a target capture rate of ~10,000 individual cells per sample. Captured mRNAs were barcoded during cDNA synthesis using the Chromium Next GEM Single-Cell 3′ GEM, Library and Gel Bead Kit v3.1 (10X Genomics) according to the manufacturer's instructions. The resulting libraries were prepared in parallel in one single batch. We pooled all of the libraries for sequencing in an Illumina

flow cell. All the libraries were sequenced with an 8-base index read, a 28-base Read1 containing cell-identifying barcodes and unique molecular identifiers (UMI), and a 91-base Read2 containing transcript sequences on an Illumina NovaSeq 6000 at Gustave Roussy.

Statistical Assessment of Single-Cell RNA Sequencing

Quality Control, Pseudomapping, and Quantification. Raw binary base call (BCL) files were demultiplexed and converted to Fastq format using bcl2fastq (Illumina). Quality control of reads was performed using fastqc and assignment to the expected genome species evaluated with fastq screen (56). Reads were pseudomapped to the Ensembl reference transcriptome v99 corresponding to the mus musculus GRCm38 build with kallisto using its « bus » subcommand and parameters corresponding to the 10X Chromium 3′ scRNA-Seq v3 chemistry (57). The index was made with the kb-python wrapper of kallisto (57, 58). Barcode correction using whitelist provided by the manufacturer (10X Genomics), and gene-based quantification of reads was performed with BUStools (59).

Quality Control on Each Sample. Cell barcodes by symbol count table were loaded in R (v3.6.3) using the BUSpaRse package (https://github.com/qubvel/segmentation_models). To call real cells from empty droplets, we used the emptyDrops() function from the dropletUtils package, which assesses whether the RNA content associated with a cell barcode is significantly distinct from the ambient background RNA present within each sample (60, 61). Barcodes with $P < 0.001$ (Benjamini–Hochberg-corrected) were considered as legitimate cells for further analysis. The count matrix was filtered to exclude genes detected in fewer than five cells, cells with fewer than 1,500 UMIs, or fewer than 200 detected genes, as well as cells with a mitochondrial transcript proportion higher than 20%. The proportion of ribosomal gene counts and the proportion of mechanical stress-response gene counts were also estimated but not used to filter cells.

Cell-Cycle Scoring. Cell-cycle scoring of each cell was performed using two methods: the cell-cycle scoring function from the Seurat package and the cyclone function from Scran. Barcodes corresponding to doublet cells were identified and discarded using the union of two methods. First, scDblFinder using default parameters except for minClusSize (set to the minimum of 50, or the number of cells divided by 50) and dbr set to (number of cells)²/1E+05). Second, *scds* with its hybrid method using default parameters (62). We manually verified that the cells identified as doublets did not systematically correspond to cells in the G_2–M phase.

Individual Analysis. Seurat was applied for further data processing. The SCTransform normalization method (63) was used to normalize, scale, select 3,000 highly variable genes, and regress out bias factors (number of detected genes, proportion of mitochondrial transcripts, proportion of ribosomal transcripts, and proportion of mechanical stress-response transcripts). Pearson residuals from this regression were used for dimension reduction by principal components analysis (PCA). The number of PCA dimensions to keep for further analysis was evaluated by assessing a range of reduced PCA spaces using 3 to 49 dimensions, with a step of 2. For each generated PCA space, Louvain clustering of cells was performed using a range of values for the resolution parameter from 0.1 to 1.2, with a step of 0.1. The optimal space was manually evaluated as the one combination of kept dimensions and clustering resolution resolving the best structure (clusters homogeneity and compacity) in a uniform manifold approximation and projection (UMAP) space. Additionally, we used the clustree method to assess if the selected optimal space corresponded to a relatively stable position in the clustering results tested for these dimensions/resolution combinations (64).

Detected clusters were mapped to known markers of IECs (13) and immune cells (65). Data sets were divided into two data sets containing either epithelial cells or immune cells based on *Ptprc* (CD45) gene expression prior to integration.

Integration Analysis. Data sets were integrated using canonical correlation analysis to identify pairwise anchors between data sets and using the anchors to harmonize the data sets, as implemented in Seurat. In practice, data sets were normalized independently using SCTransform, as described before (see individual analysis section). The top 3,000 highly variable genes across all samples were selected by the SelectIntegrationFeatures function and used for integration with the PrepSCTIntegration, FindIntegrationAnchors, and IntegrateData functions (with default parameters). After integration, a PCA was performed on the integrated data set.

Louvain clustering was performed as described for individual analysis, using 35 dimensions and a resolution of 0.9. Results were visualized through a UMAP reduction at two dimensions.

The automatic annotation of cell types, cluster marker gene detection, and cerebro visualization steps were performed similarly to the individual analysis.

Grouped analysis: IndivNorm: Each data set was normalized independently by SCTransform, as described in the individual analysis section, and then data were merged using the merge function from Seurat. A common dimension reduction was performed by PCA. Louvain clustering was performed as described for individual analysis, using 35 dimensions and a resolution of 0.9. Results were visualized through a UMAP reduction at two dimensions. The automatic annotation of cell types, cluster marker gene detection, and cerebro visualization steps were performed similarly to the individual analysis.

GlobalNorm: Data sets were merged by merge function from Seurat, and then a normalization by SCTransform and a common dimension reduction by PCA were performed (as described in the individual analysis section). Louvain clustering was performed as described for individual analysis, using 35 dimensions and a resolution of 0.9 (for the epithelial cells data set) and using 30 dimensions and a resolution of 0.9 (for the immune cells data set). Results were visualized through a UMAP reduction at two dimensions. The automatic annotation of cell types, cluster marker gene detection, and cerebro visualization steps were performed similarly to the individual analysis.

Custom differential analysis: Differential expression analyses were performed using the Wilcoxon test implemented in the Seurat package. Resulting *P* values were corrected for false-positive rate using the Bonferroni correction.

Gene set enrichment analysis: Gene set enrichment analysis was performed using fgsea R package. Pathways were retrieved from the Reactome database (https://reactome.org/) using the function Reactomepathway from fgsea package. Pathways that comprised fewer than 15 genes were excluded from the analysis.

Serum Levels of Soluble ST2, CD14, and Corticosteroids

Blood taken from mice was centrifuged for 3 minutes at 12 rcf. The serum was collected and stored at –20°C until analysis. ST2, CD14, and corticosteroid levels were measured using the Duoset murine ST2 and CD14 ELISA Kit (R&D Systems) following the manufacturer's instructions.

DNA Extraction and 16S rRNA Sequencing of Mouse Stools

Preparation and sequencing of mouse fecal samples were performed at IHU Méditerranée Infection, Marseille, France. Briefly, DNA was extracted using two protocols. The first protocol consisted of physical and chemical lysis, using glass powder and proteinase K, respectively, then processing using the Macherey-Nagel DNA Tissue Extraction Kit (66). The second protocol was identical to the first protocol, with

the addition of glycoprotein lysis and deglycosylation steps (67). The resulting DNA was sequenced, targeting the V3–V4 regions of the 16S rRNA gene as previously described (68). Raw FASTQ files were analyzed with Mothur pipeline v.1.39.5 for quality check and filtering (sequencing errors, chimerae) on a Workstation DELL T7910. Raw reads were filtered and clustered into Operational Taxonomic Units (OTU), followed by elimination of low-populated OTUs (until five reads) and by *de novo* OTU picking at 97% pairwise identity using standardized parameters and SILVA rDNA Database v.1.19 for alignment. Sample coverage was computed with Mothur and resulted to be on average higher than 99% for all samples, thus meaning a suitable normalization procedure for subsequent analyses. Bioinformatic and statistical analyses on recognized OTUs were performed with Python v.2.7.11. The most representative and abundant read within each OTU (as evidenced in the previous step with Mothur v.1.39.5) underwent a nucleotide Blast using the National Center for Biotechnology Information (NCBI) Blast software (ncbi-blast-2.3.0) and the latest NCBI 16S Microbial722 database accessed at the end of April 2019 (ftp://ftp.ncbi.nlm.nih.gov/). A matrix of bacterial relative abundances was built at each taxon level (phylum, class, order, family, genus, and species) for subsequent multivariate statistical analyses. Raw data were first normalized and then standardized using QuantileTransformer and StandardScaler methods from Sci-Kit learn package v0.20.3. Normalization transforms each variable to a strictly Gaussian-shaped distribution, whereas the standardization results in each normalized variable having a mean of zero and variance of one. These two steps of normalization followed by standardization ensure the proper comparison of variables with different dynamic ranges, such as bacterial relative abundances, tumor size, or colonic infiltrate score. Measurements of α diversity (within sample diversity), such as observed_otus and Shannon index, were calculated at the OTU level using the SciKit learn package v.0.4.1. Exploratory analysis of β-diversity (between sample diversity) was calculated using the Bray–Curtis measure of dissimilarity calculated with Mothur and represented in PCoA, whereas for hierarchical clustering analysis, the "Bray–Curtis" metrics and "complete linkage" method were implemented using custom scripts (Python v.2.7.11). We implemented PLS-DA and the subsequent variable importance plot (VIP) as a supervised analysis in order to identify the most discriminant bacterial species among the different cohorts of mice according to various therapies. When needed, univariate/multivariate statistics and correlation analyses were performed with Python v2.7 and related packages (Scipy, SciKit-learn). All *P* values were considered statistically significant if less than or equal to 0.05.

16S rRNA Gene Sequence Processing and Analysis in Mice with or without Propranolol (Supplementary Fig. S6A and S6B). Demultiplexed raw sequence data were processed using Qiime2 version 2020.6.0 along with the plugin DADA2 (69). Amplicon sequence variants (ASV) were generated for each sample. Each run was denoised separately. Briefly, sequences were corrected for Illumina amplicon sequence errors, dereplicated, and merged of paired-end reads. Figaro (70) was used to determine the optimal truncation parameters. Thus, sequence lengths were truncated at position 243 for forward reads and at position 239 for reverse reads. Runs were merged together using the qiime2's plugin feature table followed by chimera removal using uchime *de novo* method. The taxonomy assignment was performed against the GreenGenes reference database v13.8 (V3-V4 segment; ref. 71). Qiime's artifact files related to feature and taxonomy tables resp. phylogenetic tree were exported to biom respectively. Newick format in order to use with phyloseq R package v1.32 (72). For alpha-diversity analysis, each sample was downsampled to 10,000 reads (graphically determined through rarefaction curves). Samples for which reads number was below this threshold were excluded. Alpha diversity measures the species richness within each sample, which were assessed by observed ASV, Chao1, Shannon index, and inverse Simpson index. The Wilcoxon test was used to determine significant differences in alpha diversity among the two groups. β-Diversity was analyzed through PCoA with weighted UniFrac distance (73). Permutation multivariate analysis of variance using the distance metrices method (74) was used to test for the differences among communities. The DESeq2 (75) method was used for differential analysis. ASVs detected in less than 30% of samples within one group were excluded from differential analysis. All statistical analyses were performed under R version 4.0.2.

Handling of Patient Specimens

Feces-related translational research was conducted according to the ethical guidelines and approval of the local ethical committee (CCPPRB, Kremlin Bicêtre). Feces (for MG analysis) and serum collection were performed under the study "Oncobiotics," B2M ethics protocol number PP: 15-013. Written informed consent was obtained for all patients in accordance with the Declaration of Helsinki.

Clinical Management. Detailed in Supplementary Tables S1, S2, and S3. Most if not all patients were under routine clinical management outside of clinical protocols.

MG Analyses. Stool DNA extraction and sequencing have been handled by Metagenopolis platform, INRAE, Jouy-en Josas, as previously described (1, 28).

Small Intestine Crypt Isolation and Organoid Culture for Quantification of REG3γ Secretion

Crypt isolation and organoid culture were performed as previously described (76) with the following modifications. Briefly, the ileum of 10- to 13-week-old mice was cut longitudinally and scraped with a cover slip to remove villi. The intestine was cut transversely into 2- to 4-mm pieces and washed four times with cold PBS. Fragments were then incubated in 2 mmol/L EDTA in PBS for 30 minutes on ice. Following the removal of the EDTA medium, fragments were vigorously resuspended in PBS containing 10% FCS (Gibco) and passed through a 70-μm strainer (BD Bioscience). This step was repeated three times. Isolated crypts were pelleted and washed in Advanced DMEM/F12 (ADF; Invitrogen). Crypts were then resuspended in 1 mL of Matrigel growth factor reduced basement membrane matrix (Corning), and 50 μL drops were placed into prewarmed 24-well plates. Following Matrigel polymerization, crypts were overlaid with ADF supplemented with 100 U/mL penicillin G sodium, 100 μg/mL streptomycin sulfate, 2 mmol/L L-glutamine, 10 mmol/L HEPES, 1× N2 15 supplement, 1× B27 supplement, 50 ng/mL mEGF, 100 ng/mL mNoggin (PeproTech), N-acetylcysteine (Sigma; reagents from Invitrogen unless otherwise indicated), and 10% conditioned medium of R-Spondin-1–transfected HEK 293T cells. Media were changed every two to three days. Cultures were split every 7 to 10 days by first dissolving the Matrigel with cold ADF and mechanically disrupting the organoids using a narrowed Pasteur pipette. Media were supplemented five days after splitting with either adrenaline, noradrenaline, or dopamine (kind gift of the pharmacy of Gustave Roussy Institute) at a concentration of 100 μmol/L or with LPS 10 ng/mL (Sigma) + LTA 10 ng/mL (Sigma). After six days of culture, media were removed and organoids were extracted from the Matrigel using organoid harvesting solution (Cultrex, catalog no. 3700-100-01). Organoids were then lysed mechanically with narrowed Pasteur pipette to collect intraluminal content, and organoid lysates were immediately frozen at –80°C. REG3γ was quantified in organoid lysates using a commercial ELISA kit (LSBio, catalog no. LS-F6890-1). Whole protein concentration in organoid lysates was assessed using a micro BCA protein assay kit (Thermo Fisher).

Human Enteroid Manufacturing

Materials. DAPT (catalog no. D5942), dopamine hydrochloride (catalog no. H8502), (±)-epinephrine hydrochloride (catalog no.

E4642), and L-(–)-norepinephrine (+)-bitartrate salt monohydrate (catalog no. A9512) were purchased from Sigma. WNT surrogate was purchased from U-Protein Express.

Methods

Human Ileal Organoid Experiments

Human ileal tissue was obtained with written informed consent of the patients and approval of the ethical committee of the University Medical Center Utrecht. Human ileal organoids were established and cultured as previously described (77, 78), with WNT-conditioned medium replaced by WNT surrogate 0.15 nmol/L. For analysis of *REG3G* and *DEFA5* mRNA expression, organoids were first cultured in expansion conditions for four days after dissociation. Organoids were then differentiated for four days using the niche-inspired intestinal organoid culture medium containing insulin-like growth factor-1 and fibroblast growth factor 2 as described by Fujii et al. (79) with the following changes: removal of Gastrin, replacement of WNT-conditioned medium by WNT surrogate 0.15 nmol/L, and addition of 10 μmol/L of the NOTCH signaling inhibitor DAPT. This medium enhanced differentiation toward the secretory lineage. Organoids were subsequently treated with this medium without or with 100 μmol/L epinephrine, norepinephrine, or dopamine for 24 hours or three days. RNA was harvested and isolated using the RNEasy Kit (Qiagen) according to the manufacturer's protocol. Reverse transcription was performed using M-MLV Reverse Transcriptase, RNase H Minus, and Point Mutant (Promega) according to the manufacturer's protocol. Quantitative PCR was performed using the IQ Sybr Green Supermix (Bio-Rad) and the CFX384 Touch Real-Time PCR Detection System (Bio-Rad). Gene expression was normalized to expression of the housekeeping gene *GAPDH*. The following qPCR primer sequences were used:

GAPDH; Fw (5′ → 3′); GATTTGGTCGTATTGGGCGC
Rv (5′ → 3′); TTCCCGTTCTCAGCCTTGAC
REG3G; Fw (5′ → 3′); GGTGAGGAGCATTAGTAACAGC
Rv (5′ → 3′); CCAGGGTTTAAGATGGTGGAGG
DEFA5; Fw (5′ → 3′); AGACAACCAGGACCTTGCTAT
Rv (5′ → 3′); GGAGAGGGACTCACGGGTAG

Fixed Organoid Immunostaining

Organoids were collected five to seven days after passaging. Matrigel was removed using cold ADF and mechanically disrupted using a narrowed Pasteur pipette. Disrupted organoids were washed once in cold ADF and resuspended in a medium to Matrigel ratio of 1:1 at a concentration of 2,000 organoids per mL. Organoid suspension (5 μL) was plated in 96-well plates (ibidi, catalog no. 89646). After Matrigel polymerization, organoids were cultivated for five days in ADF supplemented with 100 U/mL penicillin G sodium, 100 μg/mL streptomycin sulfate, 2 mmol/L L-glutamine, 10 mmol/L HEPES, 1× N2 15 supplement, 1× B27 supplement, 50 ng/mL mEGF, 100 ng/mL mNoggin (PeproTech), N-acetylcysteine (Sigma; reagents from Invitrogen unless otherwise indicated), and 10% conditioned medium of R-Spondin-1–transfected HEK 293T cells. Media were changed every two days. After five days of culture, organoid media were supplemented with either adrenaline, noradrenaline, or dopamine at a concentration of 100 μmol/L. After six days of culture, organoids were centrifuged at 3,000 rpm for 10 minutes at 4°C prior to fixation. Organoids were fixed in Matrigel using 4% PFA in PBS at room temperature for one hour. Organoids were permeabilized with 0.5% triton X100 (Sigma) in PBS for one hour and blocked using 0.5% triton X100 in PBS supplemented with 10% FCS for one hour. Organoids were incubated with primary antibody solution containing rabbit anti-mouse Ki-67 antibody (1:200, Abcam, ab16667) and incubated for an additional 24 hours at 4°C with secondary antibody solution containing DyLitgth550 goat anti-rabbit antibody (1:200, Abcam, ab96884) and 0.2 μg/mL DAPI (Invitrogen). Images were acquired using an sp8 confocal microscope (Leïca).

Image analysis was performed using ImageJ software.

Statistical Analyses

Mouse Models. Data analyses and representations were performed with either the statistical environment R (http://www.R-project.org/), Microsoft Excel (Microsoft Co.), or Prism 8 (GraphPad). Tumor growth in mouse models was analyzed with dedicated software (80). For comparisons of nonparametric two group parameters, the Mann–Whitney *U* test was used. Kruskal–Wallis for multiple groups was used to test differences between groups. Survival curves were estimated using the Kaplan–Meier product limit method. All tests were two-sided, and *P* values <0.05 were considered statistically significant.

MG Analyses of Human Samples. We conducted a shotgun MG-based analysis of fecal material available in the curatedMetagenomicData package by considering both newly acquired and publicly available data sets (81). More specifically, we collected the stools from patients harboring kidney cancer ($N = 69$; ref. 28), breast cancer ($N = 83$; ref. 82), lung cancer ($N = 368$; ref. 83), prostate cancer ($N = 47$), ovarian cancer ($N = 29$), and chronic myelomonocytic leukemia ($N = 17$). This collection of cancer metagenomes was integrated to 108 melanoma and 705 colon cancer samples from the publicly available database (26) and compared in terms of species-level taxonomic profiles (generated using MetaPhlAn3) with 5,570 healthy individuals coming from multiple publicly available data sets (84). We found discriminative species between cancer and healthy samples by considering LEfSe coupled to a pairwise comparison of relative taxonomic abundances (for species having a prevalence equal to or greater than 5%) using bootstrapping of two-tailed Mann–Whitney *U* tests (with 1,000 permutations and correction for continuity and ties). To limit possible batch effects as much as possible, we kept in the analysis only metagenomes with at least 10M reads. Due to the well-recognized effect of lifestyle on microbiome composition, we considered only samples coming from westernized subjects. Similarly, no ATB use was associated with all publicly available samples.

Data Availability

The data generated or analyzed during this study are included within the article, its Supplementary Information files, and public repositories. Raw metagenomic sequences are available in the Sequence Read Archive (SRA) under the Bioproject accession PRJNA785435 (human) and PRJNA785093 (mice), and raw RNA sequencing is available in the ArrayExpress under accession E-MTAB-11242 (mice; https://www.ebi.ac.uk/arrayexpress/).

Code Availability

No unique software or computational code was created for this study. Codes detailing implementation of established tools/pipelines are described in detail in the Methods section and available upon request to the corresponding author.

Authors' Disclosures

J. Fahrner reports other support from Transgene outside the submitted work. O. Kepp is a cofounder of Samsara Therapeutics. G. Kroemer reports grants from Eleor, Kaleido, Lytix Pharma, PharmaMar, Samsara Therapeutics, Sanofi, Sotio, Vascage, and Vasculox/Tioma and other support from EverImmune outside the submitted work; is on the board of directors for the Bristol Myers Squibb Foundation France; and is a scientific cofounder of EverImmune, Samsara Therapeutics, and Therafast Bio. N. Segata reports grants from Oncobiome during the conduct of the study. H. Clevers reports personal fees from Roche outside the submitted work and is an inventor on a

number of patents on an invention from his lab related to adult stem cell–based organoid technology. His employer (Royal Netherlands Academy of Arts and Sciences) has exclusively licensed these patents to an organization with which H. Clevers has no involvement. L. Zitvogel reports other support from EverImmune, grants from 9 Meters, Kaleido, and Daiichi Sankyo, and grants and personal fees from Transgene during the conduct of the study; grants from Glaxo-SmithKline, Bristol Myers Squibb, Roche, and PILEJE outside the submitted work; a patent for EP21305846 pending; and is the president of the scientific advisory board for EverImmune and of the IHU Méditerranée Infections. No disclosures were reported by the other authors.

Authors' Contributions

S. Yonekura: Conceptualization, data curation, software, formal analysis, validation, investigation, writing–original draft, project administration. **S. Terrisse:** Conceptualization, data curation, software, formal analysis, investigation, writing–original draft, project administration. **C. Alves Costa Silva:** Data curation, software, formal analysis, validation, investigation, writing–original draft. **A. Lafarge:** Resources. **V. Iebba:** Software, formal analysis, metho-dology. **G. Ferrere:** Formal analysis, methodology, involved in mouse model experiments. **A. Goubet:** Formal analysis, methodology. **J. Fahrner:** Conceptualization, formal analysis, investigation, involved in mouse model experiments. **I. Lahmar:** Software, formal analysis, methodology. **K. Ueda:** Formal analysis, investigation, involved in mouse model experiments. **G. Mansouri:** Formal analysis, involved in pathology analysis. **E. Pizzato:** Formal analysis, investigation, involved in organoid experiments. **P. Ly:** Formal analysis, investigation, involved in mouse model experiments. **M. Mazzenga:** Formal analysis, investigation, involved in mouse model experiments. **C. Thelemaque:** Formal analysis, involved in mouse model experiments. **M. Fidelle:** Resources. **F. Jaulin:** Investigation. **J. Cartry:** Data curation, investigation. **M. Deloger:** Data curation, formal analysis, methodology. **M. Aglave:** Data curation, software, formal analysis, visualization, involved in bioinformatic analysis. **N. Droin:** Software, formal analysis, supervision, visualization, methodology, involved in RNA sequencing and single-cell analysis. **P. Opolon:** Formal analysis, validation. **A. Puget:** Formal analysis, visualization, involved in pathology analysis. **F. Mann:** Formal analysis, supervision, validation, methodology, involved in pathology analysis. **M. Neunlist:** Formal analysis, supervision, validation, and methodology. **A. Bessard:** Formal analysis, validation, visualization, involved in pathology analysis. **L. Aymeric:** Project administration. **T. Matysiak-Budnik:** Data curation. **J. Bosq:** Formal analysis, supervision, validation, visualization, methodology, involved in pathology analysis. **P. Hofman:** Formal analysis, supervision, validation, visualization, methodology, involved in pathology analysis. **C.P. Duong:** Formal analysis, investigation, and visualization. **S. Ugolini:** Formal analysis, supervision, validation, methodology. **V. Quiniou:** Software, formal analysis, visualization, involved in metagenomic analysis. **S. Berrard:** Validation, writing–review and editing. **B. Ryffel:** Investigation and methodology. **O. Kepp:** Writing–review and editing. **G. Kroemer:** Conceptualization, supervision, writing–original draft, writing–review and editing. **B. Routy:** Formal analysis, investigation, writing–review and editing. **L. Lordello:** Software, formal analysis, validation, visualization, involved in pathology analysis: VAChT, ChAT, Gr1, CD8, CD34/vessels analysis. **M. Bani:** Formal analysis. **N. Segata:** Methodology. **F. Yousef Yengej:** Data curation. **H. Clevers:** Resources. **J. Scoazec:** Methodology. **E. Pasolli:** Data curation, software, formal analysis, visualization, involved in human metagenomic analysis. **L. Derosa:** Conceptualization, resources, supervision, validation, investigation, writing–original draft, project administration. **L. Zitvogel:** Conceptualization, resources, supervision, funding acquisition, validation, writing–original draft, project administration, writing–review and editing.

Acknowledgments

L. Zitvogel and G. Kroemer are supported by the Seerave Foundation, Gustave Roussy Odyssea, the Gustave Roussy Foundation, the European Union Horizon 2020 Project Oncobiome (Project Number: 825410); the RHU LUMIERE: ANR-16-RHUS-0008; the Ligue contre le Cancer (équipe labellisée); Agence Nationale de la Recherche (ANR)—Projets blancs; ANR ILEOBIOME, 19-CE15-0029-01, ANR under the frame of E-Rare-2, the ERA-Net for Research on Rare Diseases; AMMICa US23/CNRS UMS3655; Association pour la Recherche sur le Cancer (ARC); Association "Le Cancer du Sein, Parlons-en!"; Cancéropôle Ile-de-France; Chancelerie des Universités de Paris (Legs Poix), Fondation pour la Recherche Médicale (FRM); a donation by Elior; European Research Area Network on Cardiovascular Diseases (ERA-CVD, MINOTAUR); Fondation Carrefour; High-end Foreign Expert Program in China (GDW20171100085), Institut National du Cancer (INCa); Inserm (HTE); Institut Universitaire de France; LeDucq Foundation; the LabEx Immuno-Oncology (ANR-18-IDEX-0001); the SIRIC Stratified Oncology Cell DNA Repair and Tumor Immune Elimination (SOCRATE); and the SIRIC Cancer Research and Personalized Medicine (CARPEM). This work is supported by the Prism project funded by the Agence Nationale de la Recherche under grant number ANR-18-IBHU-0002. F. Mann is supported by INCa, la Ligue contre le cancer, and Fondation ARC (PAIR PANCREAS 186738). S. Terrisse is financially supported by INSERM-PLAN CANCER. S. Yonekura, B. Routy, and L. Derosa were funded by Gustave Roussy Course of Excellence in Oncology–Fondation Philanthropia. O. Kepp is supported by the DIM ELICIT initiative of the Ile de France.

REFERENCES

1. Routy B, Le Chatelier E, Derosa L, Duong CPM, Alou MT, Daillère R, et al. Gut microbiome influences efficacy of PD-1–based immunotherapy against epithelial tumors. Science 2018;359:91–7.
2. Gopalakrishnan V, Spencer CN, Nezi L, Reuben A, Andrews MC, Karpinets TV, et al. Gut microbiome modulates response to anti–PD-1 immunotherapy in melanoma patients. Science 2018;359:97–103.
3. Matson V, Fessler J, Bao R, Chongsuwat T, Zha Y, Alegre M-L, et al. The commensal microbiome is associated with anti–PD-1 efficacy in metastatic melanoma patients. Science 2018;359:104–8.
4. Zitvogel L, Ma Y, Raoult D, Kroemer G, Gajewski TF. The microbiome in cancer immunotherapy: diagnostic tools and therapeutic strategies. Science 2018;359:1366–70.
5. Derosa L, Routy B, Desilets A, Daillère R, Terrisse S, Kroemer G, et al. Microbiota-centered interventions: the next breakthrough in immuno-oncology? Cancer Discov 2021;11:2396–412.
6. Derosa L, Hellmann MD, Spaziano M, Halpenny D, Fidelle M, Rizvi H, et al. Negative association of antibiotics on clinical activity of immune checkpoint inhibitors in patients with advanced renal cell and non-small-cell lung cancer. Ann Oncol 2018;29:1437–44.
7. Daillère R, Derosa L, Bonvalet M, Segata N, Routy B, Gariboldi M, et al. Trial watch: the gut microbiota as a tool to boost the clinical efficacy of anticancer immunotherapy. OncoImmunology 2020;9:1774298.
8. Hakozaki T, Richard C, Elkrief A, Hosomi Y, Benlaïfaoui M, Mimpen I, et al. The gut microbiome associates with immune checkpoint inhibition outcomes in patients with advanced non–small cell lung cancer. Cancer Immunol Res 2020;8:1243–50.
9. Singh V, Sadler R, Heindl S, Llovera G, Roth S, Benakis C, et al. The gut microbiome primes a cerebroprotective immune response after stroke. J Cereb Blood Flow Metab 2018;38:1293–8.

10. Stanley D, Mason LJ, Mackin KE, Srikhanta YN, Lyras D, Prakash MD, et al. Translocation and dissemination of commensal bacteria in post-stroke infection. Nat Med 2016;22:1277–84.
11. Mehraj V, Jenabian M-A, Ponte R, Lebouché B, Costiniuk C, Thomas R, et al. The plasma levels of soluble ST2 as a marker of gut mucosal damage in early HIV infection: AIDS 2016;30:1617–27.
12. Koebel CM, Vermi W, Swann JB, Zerafa N, Rodig SJ, Old LJ, et al. Adaptive immunity maintains occult cancer in an equilibrium state. Nature 2007;450:903–7.
13. Haber AL, Biton M, Rogel N, Herbst RH, Shekhar K, Smillie C, et al. A single-cell survey of the small intestinal epithelium. Nature 2017;551:333–9.
14. Abreu MT. Toll-like receptor signalling in the intestinal epithelium: how bacterial recognition shapes intestinal function. Nat Rev Immunol 2010;10:131–44.
15. Söderholm JD, Perdue MH. Stress and intestinal barrier function: II. Stress and intestinal barrier function. Am J Physiol Gastrointest Liver Physiol 2001;280:G7–13.
16. Zheng G, Wu S-P, Hu Y, Smith DE, Wiley JW, Hong S. Corticosterone mediates stress-related increased intestinal permeability in a region-specific manner: corticosterone and colon tight junction protein. Neurogastroenterol Motil 2013;25:e127–39.
17. Furness JB. The enteric nervous system and neurogastroenterology. Nat Rev Gastroenterol Hepatol 2012;9:286–94.
18. Tallini YN, Shui B, Greene KS, Deng K-Y, Doran R, Fisher PJ, et al. BAC transgenic mice express enhanced green fluorescent protein in central and peripheral cholinergic neurons. Physiol Genomics 2006;27:391–7.
19. Han SJ, Kim M, D'Agati VD, Lee HT. Norepinephrine released by intestinal Paneth cells exacerbates ischemic AKI. Am J Physiol Renal Physiol 2020;318:F260–72.
20. Yang S, Koo DJ, Zhou M, Chaudry IH, Wang P. Gut-derived norepinephrine plays a critical role in producing hepatocellular dysfunction during early sepsis. Am J Physiol Gastrointest Liver Physiol 2000;279:G1274–81.
21. Kokolus KM, Zhang Y, Sivik JM, Schmeck C, Zhu J, Repasky EA, et al. Beta blocker use correlates with better overall survival in metastatic melanoma patients and improves the efficacy of immunotherapies in mice. OncoImmunology 2018;7:e1405205.
22. Collins JR. Small intestinal mucosal damage with villous atrophy: a review of the literature. Am J Clin Pathol 1965;44:36–44.
23. Wangel AG, Deller DJ. Malabsorption syndrome associated with carcinoma of the bronchus. Gut 1965;6:73–6.
24. Gilat T, Fischel B, Danon J, Loewenthal M. Morphology of small bowel mucosa in malignancy. Digestion 1972;7:147–55.
25. Bindels LB, Neyrinck AM, Loumaye A, Catry E, Walgrave H, Cherbuy C, et al. Increased gut permeability in cancer cachexia: mechanisms and clinical relevance. Oncotarget 2018;9:18224–38.
26. Thomas AM, Manghi P, Asnicar F, Pasolli E, Armanini F, Zolfo M, et al. Metagenomic analysis of colorectal cancer datasets identifies cross-cohort microbial diagnostic signatures and a link with choline degradation. Nat Med 2019;25:667–78.
27. Segata N, Izard J, Waldron L, Gevers D, Miropolsky L, Garrett WS, et al. Metagenomic biomarker discovery and explanation. Genome Biol 2011;12:R60.
28. Derosa L, Routy B, Fidelle M, Iebba V, Alla L, Pasolli E, et al. Gut bacteria composition drives primary resistance to cancer immunotherapy in renal cell carcinoma patients. Eur Urol 2020;78:195–206.
29. Cardoso-Silva D, Delbue D, Itzlinger A, Moerkens R, Withoff S, Branchi F, et al. Intestinal barrier function in gluten-related disorders. Nutrients 2019;11:2325.
30. Moriyama S, Brestoff JR, Flamar A-L, Moeller JB, Klose CSN, Rankin LC, et al. β_2-adrenergic receptor–mediated negative regulation of group 2 innate lymphoid cell responses. Science 2018;359:1056–61.
31. Enaud R, Hooks KB, Barre A, Barnetche T, Hubert C, Massot M, et al. Intestinal inflammation in children with cystic fibrosis is associated with Crohn's-like microbiota disturbances. J Clin Med 2019;8:645.
32. Bindels LB, Neyrinck AM, Claus SP, Le Roy CI, Grangette C, Pot B, et al. Synbiotic approach restores intestinal homeostasis and prolongs survival in leukaemic mice with cachexia. ISME J 2016;10:1456–70.
33. Bindels LB, Neyrinck AM, Salazar N, Taminiau B, Druart C, Muccioli GG, et al. Non digestible oligosaccharides modulate the gut microbiota to control the development of leukemia and associated cachexia in mice. PLoS One 2015;10:e0131009.
34. Bohórquez DV, Shahid RA, Erdmann A, Kreger AM, Wang Y, Calakos N, et al. Neuroepithelial circuit formed by innervation of sensory enteroendocrine cells. J Clin Invest 2015;125:782–6.
35. Pavlov VA, Wang H, Czura CJ, Friedman SG, Tracey KJ. The cholinergic anti-inflammatory pathway: a missing link in neuroimmunomodulation. Mol Med Camb Mass 2003;9:125–34.
36. Bansal V, Costantini T, Ryu SY, Peterson C, Loomis W, Putnam J, et al. Stimulating the central nervous system to prevent intestinal dysfunction after traumatic brain injury: J Trauma Inj Infect Crit Care 2010;68:1059–64.
37. Singh V, Roth S, Llovera G, Sadler R, Garzetti D, Stecher B, et al. Microbiota dysbiosis controls the neuroinflammatory response after stroke. J Neurosci 2016;36:7428–40.
38. Wong CHY, Jenne CN, Lee W-Y, Leger C, Kubes P. Functional innervation of hepatic iNKT cells is immunosuppressive following stroke. Science 2011;334:101–5.
39. Roth S, Singh V, Tiedt S, Schindler L, Huber G, Geerlof A, et al. Brain-released alarmins and stress response synergize in accelerating atherosclerosis progression after stroke. Sci Transl Med 2018;10:eaao1313.
40. Staedtke V, Bai R-Y, Kim K, Darvas M, Davila ML, Riggins GJ, et al. Disruption of a self-amplifying catecholamine loop reduces cytokine release syndrome. Nature 2018;564:273–7.
41. Tutton PJ, Helme RD. Stress induced inhibition of jejunal crypt cell proliferation. Virchows Arch B Cell Pathol 1973;15:23–34.
42. Tutton PJM, Barkla DH. Effect of an inhibitor of noradrenaline uptake, desipramine, on cell proliferation in the intestinal crypt epithelium. Virchows Arch B Cell Pathol Incl Mol Pathol 1989;57:349–52.
43. De Schepper S, Verheijden S, Aguilera-Lizarraga J, Viola MF, Boesmans W, Stakenborg N, et al. Self-maintaining gut macrophages are essential for intestinal homeostasis. Cell 2018;175:400–15.
44. Muller PA, Koscsó B, Rajani GM, Stevanovic K, Berres M-L, Hashimoto D, et al. Crosstalk between muscularis macrophages and enteric neurons regulates gastrointestinal motility. Cell 2014;158:300–13.
45. Gabanyi I, Muller PA, Feighery L, Oliveira TY, Costa-Pinto FA, Mucida D. Neuro-immune interactions drive tissue programming in intestinal macrophages. Cell 2016;164:378–91.
46. Matheis F, Muller PA, Graves CL, Gabanyi I, Kerner ZJ, Costa-Borges D, et al. Adrenergic signaling in muscularis macrophages limits infection-induced neuronal loss. Cell 2020;180:64–78.
47. Muller PA, Schneeberger M, Matheis F, Wang P, Kerner Z, Ilanges A, et al. Microbiota modulate sympathetic neurons via a gut–brain circuit. Nature 2020;583:441–6.
48. Prüss H, Tedeschi A, Thiriot A, Lynch L, Loughhead SM, Stutte S, et al. Spinal cord injury-induced immunodeficiency is mediated by a sympathetic-neuroendocrine adrenal reflex. Nat Neurosci 2017;20:1549–59.
49. Obata Y, Castaño Á, Boeing S, Bon-Frauches AC, Fung C, Fallesen T, et al. Neuronal programming by microbiota regulates intestinal physiology. Nature 2020;578:284–9.
50. Kaelberer MM, Buchanan KL, Klein ME, Barth BB, Montoya MM, Shen X, et al. A gut-brain neural circuit for nutrient sensory transduction. Science 2018;361:eaat5236.
51. Chiu IM, Heesters BA, Ghasemlou N, Von Hehn CA, Zhao F, Tran J, et al. Bacteria activate sensory neurons that modulate pain and inflammation. Nature 2013;501:52–7.
52. Amit M, Takahashi H, Dragomir MP, Lindemann A, Gleber-Netto FO, Pickering CR, et al. Loss of p53 drives neuron reprogramming in head and neck cancer. Nature 2020;578:449–54.
53. Magnon C, Hall SJ, Lin J, Xue X, Gerber L, Freedland SJ, et al. Autonomic nerve development contributes to prostate cancer progression. Science 2013;341:1236361.
54. Hamy A-S, Derosa L, Valdelièvre C, Yonekura S, Opolon P, Priour M, et al. Comedications influence immune infiltration and pathological response to neoadjuvant chemotherapy in breast cancer. OncoImmunology 2020;9:1677427.
55. Bankhead P, Loughrey MB, Fernández JA, Dombrowski Y, McArt DG, Dunne PD, et al. QuPath: open source software for digital pathology image analysis. Sci Rep 2017;7:16878.

56. Wingett SW, Andrews S. FastQ screen: a tool for multi-genome mapping and quality control. F1000Research 2018;7:1338.
57. Bray NL, Pimentel H, Melsted P, Pachter L. Near-optimal probabilistic RNA-seq quantification. Nat Biotechnol 2016;34:525–7.
58. Melsted P, Booeshaghi AS, Gao F, Beltrame E, Lu L, Hjorleifsson KE, et al. Modular and efficient pre-processing of single-cell RNA-seq. BioRxiv 673285 [Preprint]. 2019. Available from: https://doi.org/10.1101/673285.
59. Melsted P, Ntranos V, Pachter L. The barcode, UMI, set format and BUStools. Bioinformatics 2019;35:4472–3.
60. Lun ATL, Riesenfeld S, Andrews T, Dao TP, Gomes T, participants in the 1st Human Cell Atlas Jamboree, et al. EmptyDrops: distinguishing cells from empty droplets in droplet-based single-cell RNA sequencing data. Genome Biol 2019;20:63.
61. Griffiths JA, Richard AC, Bach K, Lun ATL, Marioni JC. Detection and removal of barcode swapping in single-cell RNA-seq data. Nat Commun 2018;9:2667.
62. Bais AS, Kostka D. scds: computational annotation of doublets in single-cell RNA sequencing data. Bioinformatics 2020;36:1150–8.
63. Hafemeister C, Satija R. Normalization and variance stabilization of single-cell RNA-seq data using regularized negative binomial regression. Genome Biol 2019;20:296.
64. Zappia L, Oshlack A. Clustering trees: a visualization for evaluating clusterings at multiple resolutions. GigaScience 2018;7:giy083.
65. Xu H, Ding J, Porter CBM, Wallrapp A, Tabaka M, Ma S, et al. Transcriptional atlas of intestinal immune cells reveals that neuropeptide α-CGRP modulates group 2 innate lymphoid cell responses. Immunity 2019;51:696–708.
66. Dridi B, Henry M, El Khéchine A, Raoult D, Drancourt M. High prevalence of methanobrevibacter smithii and methanosphaera stadtmanae detected in the human gut using an improved DNA detection protocol. PLoS One 2009;4:e7063.
67. Angelakis E, Bachar D, Henrissat B, Armougom F, Audoly G, Lagier J-C, et al. Glycans affect DNA extraction and induce substantial differences in gut metagenomic studies. Sci Rep 2016;6:26276.
68. Million M, Tidjani Alou M, Khelaifia S, Bachar D, Lagier J-C, Dione N, et al. Increased gut redox and depletion of anaerobic and methanogenic prokaryotes in severe acute malnutrition. Sci Rep 2016;6:26051.
69. Callahan BJ, McMurdie PJ, Rosen MJ, Han AW, Johnson AJA, Holmes SP. DADA2: high-resolution sample inference from Illumina amplicon data. Nat Methods 2016;13:581–3.
70. Weinstein MM, Prem A, Jin M, Tang S, Bhasin JM. FIGARO: An efficient and objective tool for optimizing microbiome rRNA gene trimming parameters [Internet]. Bioinformatics; 2019. Available from: http://biorxiv.org/lookup/doi/10.1101/610394.
71. McDonald D, Price MN, Goodrich J, Nawrocki EP, DeSantis TZ, Probst A, et al. An improved Greengenes taxonomy with explicit ranks for ecological and evolutionary analyses of bacteria and archaea. ISME J 2012;6:610–8.
72. McMurdie PJ, Holmes S. phyloseq: an R package for reproducible interactive analysis and graphics of microbiome census data. PLoS One 2013;8:e61217.
73. Lozupone CA, Hamady M, Kelley ST, Knight R. Quantitative and qualitative β diversity measures lead to different insights into factors that structure microbial communities. Appl Environ Microbiol 2007;73:1576–85.
74. McArdle BH, Anderson MJ. Fitting multivariate models to community data: a comment on distance-based redundancy analysis. Ecology 2001;82:290–7.
75. Love MI, Huber W, Anders S. Moderated estimation of fold change and dispersion for RNA-seq data with DESeq2. Genome Biol 2014;15:550.
76. Sato T, Vries RG, Snippert HJ, van de Wetering M, Barker N, Stange DE, et al. Single Lgr5 stem cells build crypt-villus structures in vitro without a mesenchymal niche. Nature 2009;459:262–5.
77. Sato T, Stange DE, Ferrante M, Vries RGJ, Van Es JH, Van den Brink S, et al. Long-term expansion of epithelial organoids from human colon, adenoma, adenocarcinoma, and Barrett's epithelium. Gastroenterology 2011;141:1762–72.
78. Beumer J, Artegiani B, Post Y, Reimann F, Gribble F, Nguyen TN, et al. Enteroendocrine cells switch hormone expression along the crypt-to-villus BMP signalling gradient. Nat Cell Biol 2018;20:909–16.
79. Fujii M, Matano M, Toshimitsu K, Takano A, Mikami Y, Nishikori S, et al. Human intestinal organoids maintain self-renewal capacity and cellular diversity in niche-inspired culture condition. Cell Stem Cell 2018;23:787–93.
80. Enot DP, Vacchelli E, Jacquelot N, Zitvogel L, Kroemer G. TumGrowth: an open-access web tool for the statistical analysis of tumor growth curves. Oncoimmunology 2018;7:e1462431.
81. Pasolli E, Schiffer L, Manghi P, Renson A, Obenchain V, Truong DT, et al. Accessible, curated metagenomic data through ExperimentHub. Nat Methods 2017;14:1023–4.
82. Terrisse S, Derosa L, Iebba V, Ghiringhelli F, Vaz-Luis I, Kroemer G, et al. Intestinal microbiota influences clinical outcome and side effects of early breast cancer treatment. Cell Death Differ 2021;28:2778–96.
83. Derosa L, Routy B, Thomas AM, Iebba V, Zalcman G, Friard S, et al. Intestinal Akkermansia muciniphila predicts clinical response to PD-1 blockade in patients with advanced non-small-cell lung cancer. Nat Med 2022;28:315–24.
84. Beghini F, McIver LJ, Blanco-Míguez A, Dubois L, Asnicar F, Maharjan S, et al. Integrating taxonomic, functional, and strain-level profiling of diverse microbial communities with bioBakery 3. Elife 2021;10:e65088.